

Thermal annealing effects on $\text{La}_2\text{Hf}_2\text{O}_7:\text{Eu}^{3+}$ nanoparticles: A curious case study of structural evolution and site-specific photo- and radio-luminescence

Santosh K. Gupta^{1,2}, Jose P Zuniga¹, Maya Abdou¹, and Yuanbing Mao^{1,3*}

¹Department of Chemistry, University of Texas Rio Grande Valley, 1201 West University Drive, Edinburg, Texas 78539, USA

²Radiochemistry Division, Bhabha Atomic Research Centre, Trombay, Mumbai-400085, India

³School of Earth, Environmental, and Marine Sciences, University of Texas Rio Grande Valley, 1201 West University Drive, Edinburg, Texas 78539, USA

*To whom correspondence should be addressed. Electronic mail: yuanbing.mao@utrgv.edu, Tel.: +1-956-665-2986.

Abstract

Thermal annealing has profound effect on material characteristics such as defect, crystallinity, surface area, size, and morphology, etc., and followed with significant influence on their optoelectronic and scintillator properties. As a function of annealing temperature, our as-synthesized $\text{La}_2\text{Hf}_2\text{O}_7:\text{Eu}^{3+}$ NPs by a molten-salt method (MSS) showed a systematic increase in the quantum efficiency and emission output up to 950°C before a slight reduction at 1050°C. This phenomenon has been attributed to the decrease of surface defects as a function of annealing temperature. In addition, asymmetry ratio decreases monotonically as a function of annealing temperature and complete symmetric environment around europium was observed at 1050°C. This can be correlated with the fact that the crystal structure becomes more and more ordered (ideal pyrochlore) as the annealing temperature is increased. The sample annealed at 1050°C displayed site-specific luminescence and can be useful in designing need based orange or red phosphor. The synthesized materials show different emission characteristics in terms of asymmetry and emission output under excitation with highly energetic X-ray beam. The current work highlighted the importance of thermal treatment in modulating the light emitting properties of red phosphors and X-ray scintillators.

Keywords: Pyrochlore; Europium; Molten-salt synthesis; Lanthanum hafnate; Photoluminescence; Annealing

1. Introduction

Lanthanide based luminescent nanomaterials exhibit unique properties such as narrow emission, high color purity, millisecond lifetime, and large Stoke shift, which make them favorable for various applications such as biological imaging,¹ optical sensors,² high power LEDs,³ anti-counterfeiting,⁴ memory devices,⁵ photovoltaic cells,⁶ etc. They have favorable properties such as high thermal stability, high chemical stability, lattice stiffness, ease of synthesis, ability to accommodate lanthanides at both A and B site, and ability to tolerate both anion and cation disorder, etc.⁷ Moreover, lanthanide doped nanoparticles (NPs) are expected to behave differently from their bulk counterpart owing to confinement effect, change in electronic spectra of host matrix, and increased surface area.⁸ They could exhibit better electron-hole overlap integral and better luminescence efficiency than their bulk materials. For example, Meltzer *et al.* have reported enhanced photoluminescence efficiency in $\text{Y}_2\text{O}_3:\text{Eu}^{3+}$ nanocrystals compared to its bulk form, which is attributed to increase in radiative transition rate.⁹

Among various Ln^{3+} -doped luminescent materials, $\text{A}_2\text{B}_2\text{O}_7$ pyrochlore compounds are considered as excellent luminescence host for tunable phosphor materials.¹⁰⁻¹⁵ Generally, they exist in two structural variants: ordered pyrochlore (OP, $\text{Fd}\bar{3}m$) and disordered fluorite (DF, $\text{Fm}\bar{3}m$). There are two types of polyhedra that exist within the ideal $\text{A}_2\text{B}_2\text{O}_7$ pyrochlore lattice, 8-fold A^{3+} site and 6-fold B^{4+} site. The exact type of polyhedron formed is determined by the x coordinate of the 48f oxygen anion.¹⁶ At $x = 0.375$, the six-fold polyhedron is at its most distorted configuration, whilst the 8-fold polyhedron is a cube, which forms the defect-fluorite structure. At $x = 0.3125$, the 6-fold polyhedron forms a perfect octahedron, whilst the 8-fold polyhedron forms a distorted scalenohedra, a polyhedron where each face forms a scalene triangle, and can be viewed as a distortion of a cube which forms the ideal pyrochlore structure. Lanthanum hafnate $\text{La}_2\text{Hf}_2\text{O}_7$ is one of the most sought out pyrochlore because of its various suitable properties such as low chemical activity, low thermal conductivity, high thermal stability, phase stability over a large temperature range and high melting point.¹⁷ Due to these favorable properties, $\text{La}_2\text{Hf}_2\text{O}_7$ is used in various applications such as thermal barrier coatings and production of various refractory ceramic for aircraft.¹⁸ Also it can easily form solid solutions with actinide and possess extremely good radiation stability, which make it a suitable matrix for nuclear waste immobilization.¹⁷ Our interest in hafnate based pyrochlore materials originates from the fact that they possess high density and high atomic number (Z), which are very

important properties for designing efficient scintillating materials.^{15, 19} $\text{La}_2\text{Hf}_2\text{O}_7$ is also a very good luminescence host mainly because of two reasons: (i) no need for charge compensation as Eu^{3+} is more likely to stabilize at the La^{3+} site due to the similarity in ionic radius, and (ii) La^{3+} is not a luminescent active ion and could not give any emission due to its electronic configuration of $4d^{10}$, therefore, there will be no optical interference.^{10-15, 20-21}

Europium ion is one of the most efficient red emitting ions, which are often used commercially in light emitting diodes for solid-state lighting. It is also one of the most frequently used dopant ion as a spectroscopic probe for studying the roles of charge compensator,²² local structure,²³⁻²⁵ host-dopant energy transfer dynamics,^{24, 26-27} point group symmetry,^{10-11, 22, 27-28} low temperature luminescence dynamics,²⁹ and thermal effect,³⁰ etc. Its color output in various hosts can be tuned by optimizing the synthesis method, co-doping, host-sensitized energy transfer, dopant concentration, annealing time, and annealing temperature, etc.³¹ In terms of the optical properties of transition metal and lanthanide ion doped $\text{La}_2\text{Hf}_2\text{O}_7$, there are several research groups including ours where luminescence and scintillation properties are explored.^{13, 15, 20, 32-39} Specifically, we have synthesized $\text{La}_2\text{Hf}_2\text{O}_7:\text{Eu}^{3+}$ NPs using a combined coprecipitation and molten-salt synthesis (MSS) method at relatively low temperature of 650°C and investigated their photoluminescence (PL) and radioluminescence (RL) in recent years.^{13, 15}

In materials science, thermal annealing is a heat treatment that alters the physical and sometimes chemical properties of a material such as intrinsic stress liberation, structural improving, and surface roughness control. In annealing, atoms migrate in the crystal lattice, surface morphology modifies, and the number of dislocations decreases, leading to property change of materials, so further heat treatments of various materials with temperature and time have been used to achieve desirable properties.⁴⁰ Thermal annealing is also known to have significant influence on the luminescence properties of europium ion doped nanophosphor materials.³⁰ Exposing nanophosphors to different annealing temperatures and durations may lead to change in the size of NPs, and can also have an effect on the crystallinity of the samples and the coordination number and geometry around dopant Eu^{3+} ions.³⁰ Such changes may affect the type and density of defect in the nanomaterials.⁴¹ However, there is no systematic studies on the spectral modulation of $\text{La}_2\text{Hf}_2\text{O}_7:\text{Eu}^{3+}$ NPs by thermal treatment, not to mention correlating their structural evolution and both PL and RL performance. Therefore, in this study, we have taken Eu^{3+} as a luminescence structural probe to study the effects of thermal annealing on PL and RL

of $\text{La}_2\text{Hf}_2\text{O}_7:5\%\text{Eu}^{3+}$ NPs. The effort was taken to investigate the effect of annealing temperature on radiative transition rate, Judd-Ofelt parameters, branching ratio, asymmetry ratio, and quantum yield of $\text{La}_2\text{Hf}_2\text{O}_7:\text{Eu}^{3+}$ NPs. Structural changes induced by annealing temperature were also studied using X-ray diffraction (XRD), Raman spectroscopy, Fourier-transform infrared spectroscopy (FTIR), and BET surface area.

2. Experimental

In this work, $\text{La}_2\text{Hf}_2\text{O}_7:5\text{mol}\%\text{Eu}^{3+}$ NPs were synthesized by a molten salt method at 650°C using the mixture of NaNO_3 and KNO_3 as the salt following a previously reported procedure.¹³⁻¹⁵ More specifically, the synthesis involved two steps. First, a single-source complex precursors of $\text{La}(\text{OH})_3 \cdot 5\%\text{Eu}(\text{OH})_3 \cdot \text{HfO}(\text{OH})_2 \cdot n\text{H}_2\text{O}$ was co-precipitated using 10% $\text{NH}_4\text{OH}(\text{aq})$. Then, the single-source complex precursor was combined with a nitrate mixture ($\text{NaNO}_3:\text{KNO}_3 = 1:1$, molar ratio) by hand-grinding and heated at 650°C for 6 hours to synthesize the as-prepared $\text{La}_2\text{Hf}_2\text{O}_7:5\%\text{Eu}^{3+}$ NPs through a facile molten salt synthetic process.

To investigate the thermal annealing effects on these as-prepared $\text{La}_2\text{Hf}_2\text{O}_7:5\%\text{Eu}^{3+}$ NPs, they were further annealed at 750°C , 850°C , 950°C , and 1050°C in air for 3 hours (3 deg/min). Correspondingly, the as-prepared and post-annealed $\text{La}_2\text{Hf}_2\text{O}_7:5\%\text{Eu}^{3+}$ NPs were labeled as LHOE-AP, LHOE-750, LHOE-850, LHOE-950, and LHOE-1050, respectively.

The structure and phase purity of $\text{La}_2\text{Hf}_2\text{O}_7:\text{Eu}^{3+}$ NPs were investigated using BRUKERTM D8 X-ray Diffractometer with a $\text{Cu K}\alpha_1$ radiation ($\lambda = 0.15406$ nm, 40 kV, 40 mA). It was used with a 2θ scanning mode ranging from 10° to 90° and a scanning step size of 0.04° at a scanning rate of $2.0^\circ \text{min}^{-1}$. Rietveld refinement was carried out using PROGRAM FullProf.2k (Version 6.00 - Mar2017-ILL JRC). The refinement was carried out by varying cell parameters, position of the La, Hf, and O atoms occupancy and thermal parameters. The lattice parameters, cell volume, space group, and bond angle estimated from the refinement along with other refinement parameter is tabulated in Table S1. The structural characteristics of the europium doped $\text{La}_2\text{Hf}_2\text{O}_7$ NPs were investigated by Raman spectroscopy on a Renishaw 2000 Micro-Raman equipped with an argon laser (514.5 nm), in the range of $200\text{--}1000 \text{cm}^{-1}$. FTIR spectroscopy was obtained through a Thermo Nicolet NexusTM 470 FT-IR system. The microstructure and morphology of these NPs were studied using a Carl Zeiss sigma VP field emission scanning electron microscopy (FESEM) equipped with a field emission gun operated at 5 kV. Surface area

of the NPs was measured by nitrogen adsorption and desorption measurement (Micromeritics Instrument Corp. GEMINI VII 2390P). Photoluminescence (PL), emission, excitation, QY, and time resolved emission spectroscopy (TRES) were measured using an Edinburgh Instruments FLS 980 fluorometer system equipped with both a pulse source and a steady state source, and having a frequency range of 1-100 Hz.

3. Results and discussion

3.1 Thermal annealing effect on structural evolution

3.1.1 XRD and Rietveld refinement

Figure 1 shows the X-ray diffraction (XRD) patterns of the as-prepared (650°C) Eu^{3+} -doped $\text{La}_2\text{Hf}_2\text{O}_7$ NPs as well as with those heated at different temperatures. All the samples crystallizes in pure $\text{La}_2\text{Hf}_2\text{O}_7$ composition and it is clearly seen from these pattern that samples are crystalline in nature. The average crystallite size of The $\text{La}_2\text{Hf}_2\text{O}_7:\text{Eu}^{3+}$ NPs increased from 18 to 47 nm (Table 1) with an increase of the annealing temperature from 650 to 1050°C. This phenomenon is attributed to Ostwald ripening process wherein smaller particles gets deposited on larger particles.⁴² The growth of these NPs as a function of annealing temperature is also seen from SEM images (Figure S1). Also, it was further seen that the NPs are spherical in shape but they tend to form small clusters at higher annealing temperature.

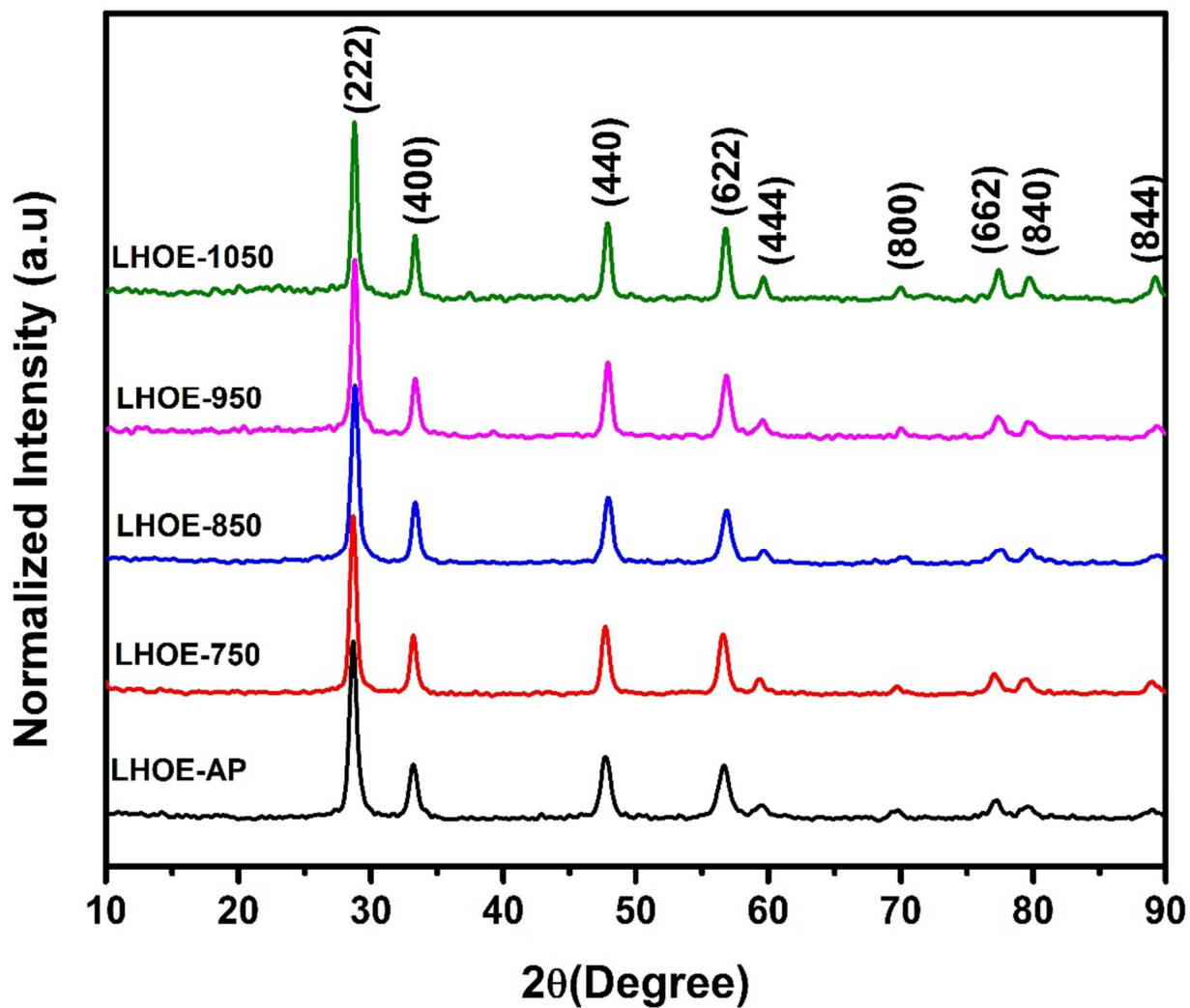
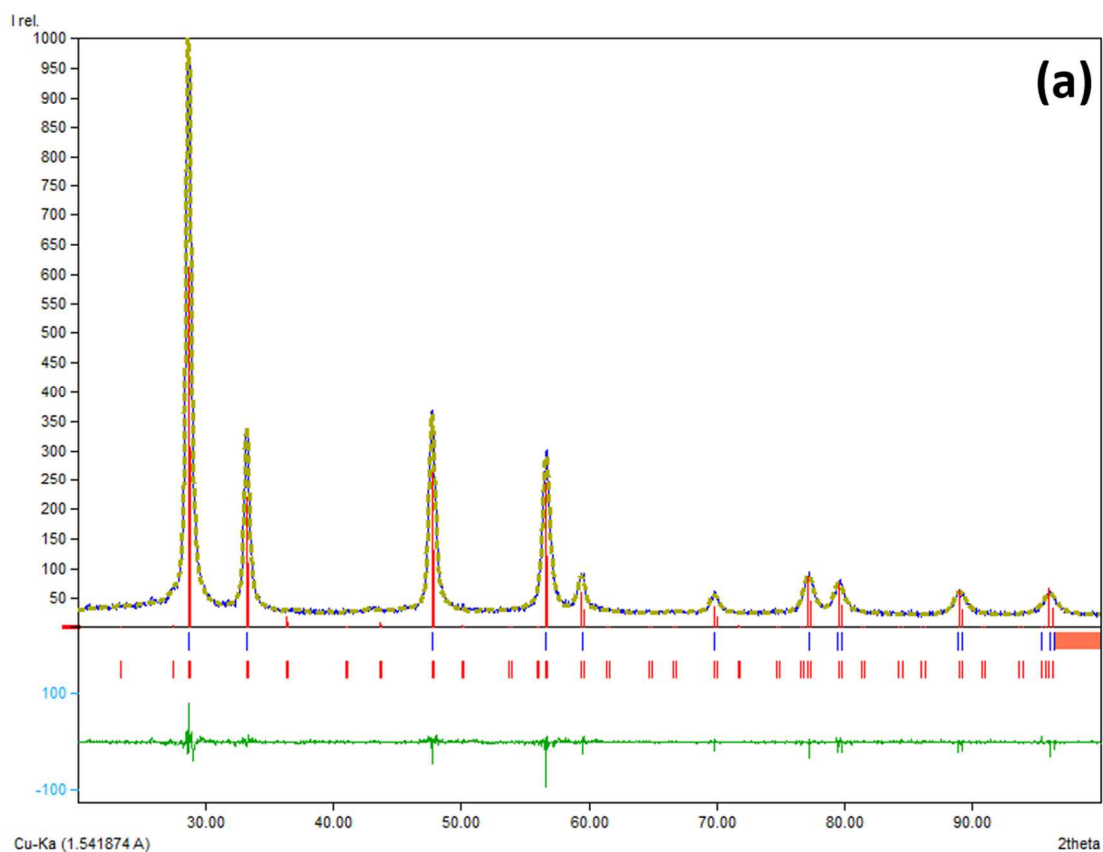


Figure 1. XRD pattern of the $\text{La}_2\text{Hf}_2\text{O}_7:\text{Eu}^{3+}$ NPs as a function of annealing temperature.

Table 1. Crystallite size of the $\text{La}_2\text{Hf}_2\text{O}_7:\text{Eu}^{3+}$ NPs as a function of annealing temperature

Samples	2θ ($^\circ$)	FWHM (β)	Crystallite size (nm)
LHOE-AP	28.66	0.43	18.48
LHOE-750	28.67	0.38	27.39
LHOE-850	28.80	0.29	20.91
LHOE-950	28.79	0.26	30.56
LHOE-1050	28.77	0.17	46.73

Figure 2 shows the Rietveld refined X-ray diffraction (XRD) patterns of the undoped and Eu^{3+} doped $\text{La}_2\text{Hf}_2\text{O}_7$ NPs. It was found that the $\text{La}_2\text{Hf}_2\text{O}_7$ and $\text{La}_2\text{Hf}_2\text{O}_7:\text{Eu}^{3+}$ NPs have crystallized in the fluorite structure with space group of Fm-3m (Figure S2a) with the lattice constants in agreement with what have been reported for $\text{La}_2\text{Hf}_2\text{O}_7$ (Table S1).⁴³ From the XRD patterns, it can also be seen that the doping of europium ion did not distort the basic fluorite network of $\text{La}_2\text{Hf}_2\text{O}_7$ that can be easily visualized using Figure 1b and Figure S2b. The chemical content of the unit cell is 16.0000 La + 48.0002 O + 16.0000 Hf + 8.0001 O. The normalized site occupation numbers in percentage are 100.0000 La1 : 100.0004 O2 : 100.0000 Hf3 : 100.0012 O4. A summary of results obtained from the Rietveld refinements is shown in Table S2.



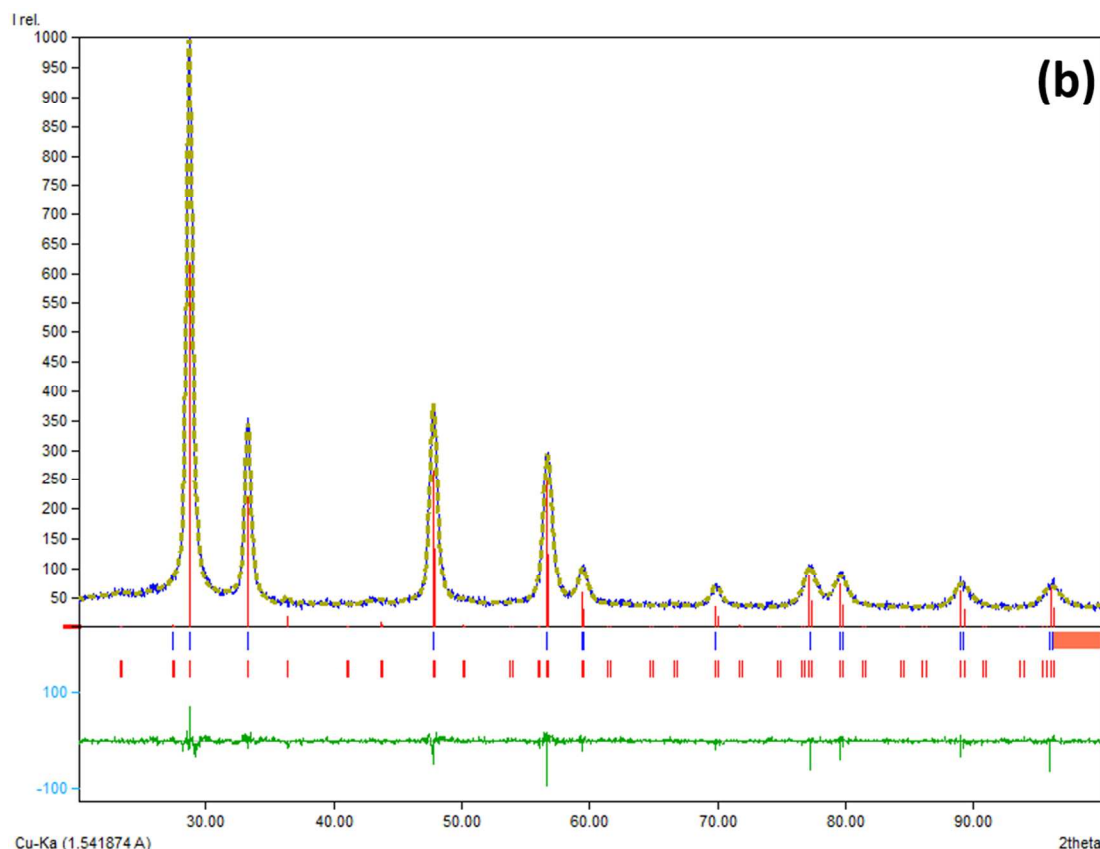


Figure 2. Rietveld refined XRD pattern of (a) undoped $\text{La}_2\text{Hf}_2\text{O}_7$ and (b) 5% Eu^{3+} doped $\text{La}_2\text{Hf}_2\text{O}_7$ NPs synthesized at 650°C .

3.1.2 Raman spectroscopy

Figure 3a shows the Raman spectra of the $\text{La}_2\text{Hf}_2\text{O}_7:\text{Eu}^{3+}$ NPs originally synthesized and annealed at different temperatures. We observed no distinct pyrochlore modes in the Raman spectrum of the LHOE-AP NPs after the original synthesis temperature at 650°C . This sample synthesized at 650°C is more like a fluorite phase which is in complete agreement with the XRD results. Annealing of the LHOE-AP sample at 750°C leads to the emergence of these pyrochlore modes. All the samples annealed at 750°C and above have Raman modes centered at 308, 323, 405, 504, 523, and 607 cm^{-1} . The Raman spectra showing deconvoluted pyrochlore peaks are shown in Figure S3. In the $\text{La}_2\text{Hf}_2\text{O}_7$ NPs, the above-mentioned peaks are attributed to vibration of La-O and Hf-O bonds. In the ideal pyrochlore $\text{A}_2\text{B}_2\text{O}_7$ type oxide, A and B cations are located at 16d and 16c sites, respectively. Since they have center of symmetry, they are reported to be Raman inactive.⁴⁴ Therefore, the observed six Raman bands are ascribed to metal ion

coordinated with the oxygen positions O_a and O_b occupying 48f and 8b sites. M- O_a vibration leads to $A_{1g} + E_g + {}^3F_{2g}$ Raman modes whereas metal- O_b vibration generates F_{2g} Raman mode. The Raman band at 757 cm^{-1} is attributed to distortion in HfO_6 octahedra. Raman spectra shown in Figure 3a suggested that for samples annealed at temperatures of 750°C and above, $\text{La}_2\text{Hf}_2\text{O}_7:\text{Eu}^{3+}$ NPs have pyrochlore-type structure with ordering of cations and oxygen vacancies. The extent of pyrochlore ordering seems to increase as the annealing temperature is increased. All six pyrochlore modes E_g (323 cm^{-1}), A_{1g} (504 cm^{-1}) and ${}^4F_{2g}$ (308 main, 405 , 523 and 607 cm^{-1}) can be clearly seen in the Raman spectra of the $\text{La}_2\text{Hf}_2\text{O}_7:\text{Eu}^{3+}$ NPs as the annealing temperature increases.⁴⁵ The as-synthesized LHOE-AP sample has short range ordering of cation and oxygen vacancies with significant fluorite contribution. However, the interesting thing is that the increase in the intensity of Raman peaks is proportional to the increment of annealing temperature, whereas FWHM of Raman modes decreases. The fluorite-pyrochlore phase transition is reported to accompany by a reduction in the width of the observed maxima corresponding to the pyrochlore Raman modes.⁴⁴ Figure 3b shows the variation of FWHM of Raman peak as a function of annealing temperature. In this analysis, the FWHM of the most intense Raman peak ($\sim 308\text{ cm}^{-1}$) was used. It can be seen that there is a progressive decrease in width of Raman peak as the annealing temperature is raised. This is attributed to the effect of phonon confinement when the particles are very small. As can be seen from the previous section that the crystalline size grows from 18 nm to 47 nm as the annealing temperature is increased to 1050°C .

Heisenberg uncertainty principle could successfully explain the phonon confinement model based on the correlation between nanoparticle size and phonon momentum distribution ($\Delta X \Delta P \geq \hbar^2/4$),⁴⁶ where ΔX is the uncertainty of nanoparticle size, ΔP is the uncertainty of phonon momentum distribution, and \hbar is the reduced Planck's constant. As the particle size decreases, phonons are increasingly confined within the particle, so phonon momentum distribution increases to cause Raman peak broadening. This phonon dispersion causes asymmetric broadening in spectral peaks and may sometime cause shift in the Raman bands.⁴⁷

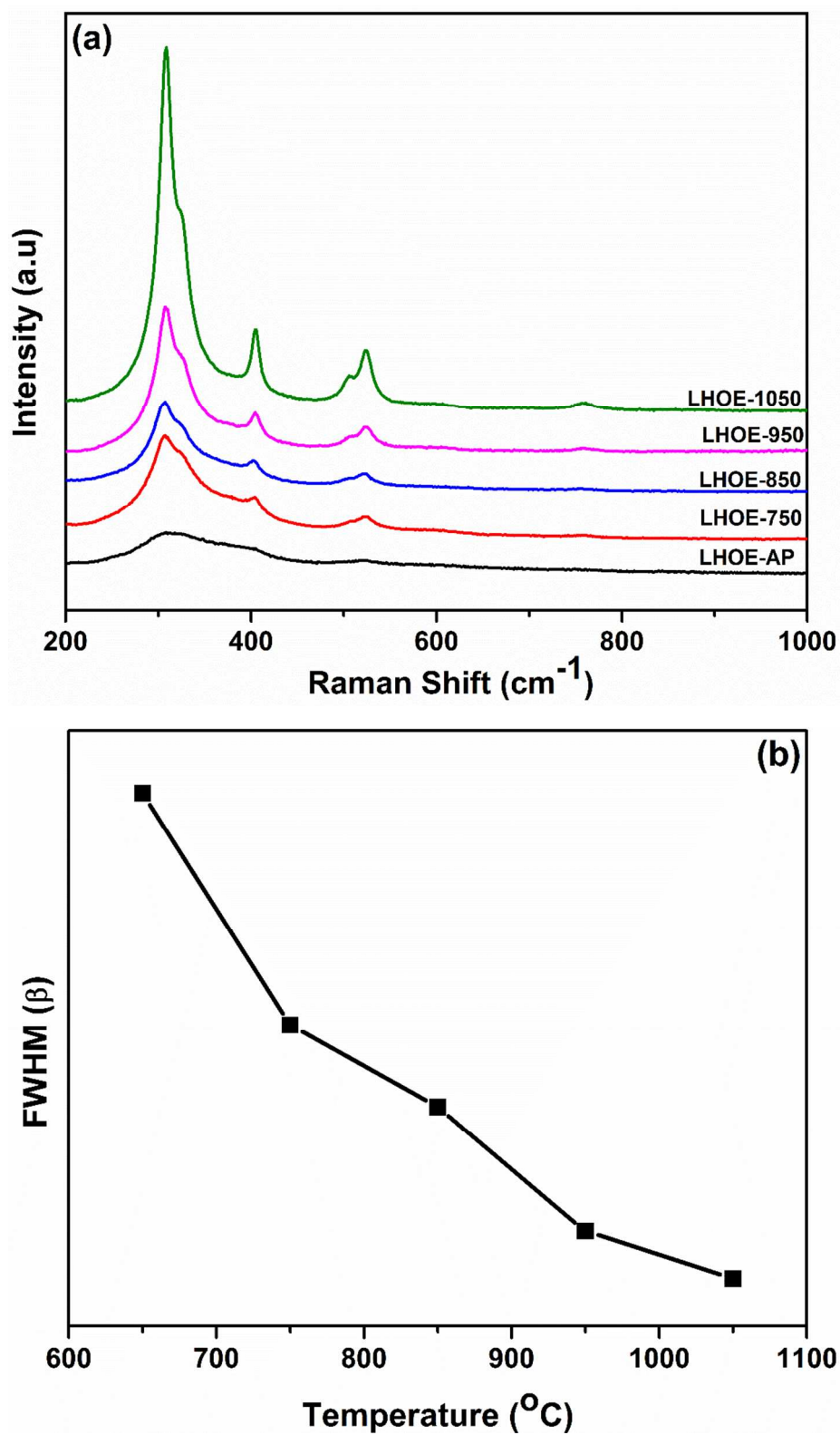
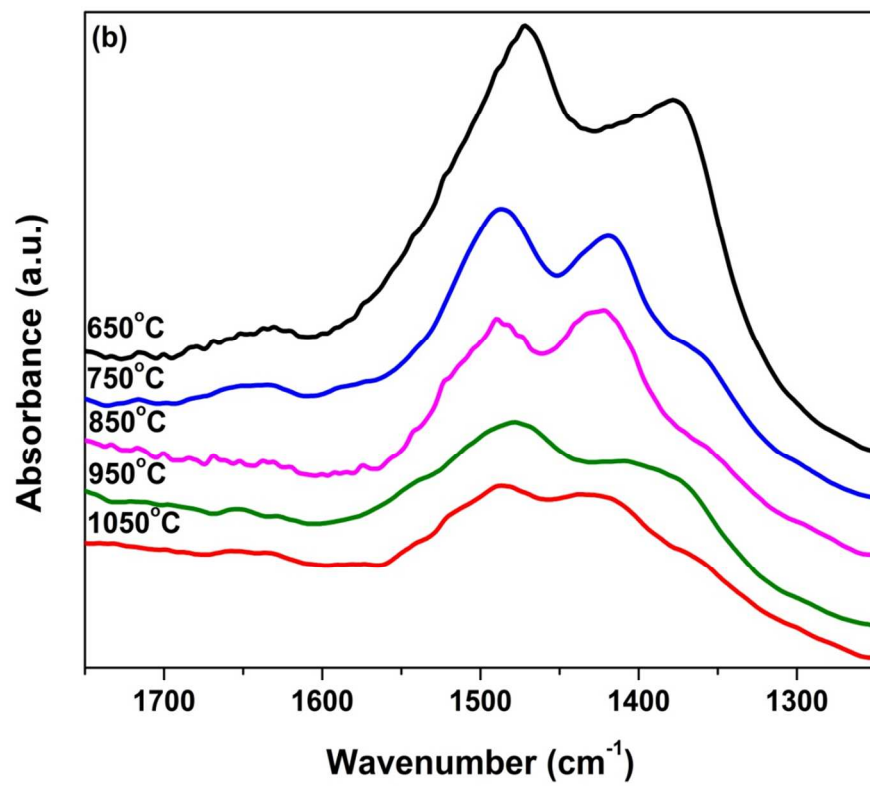
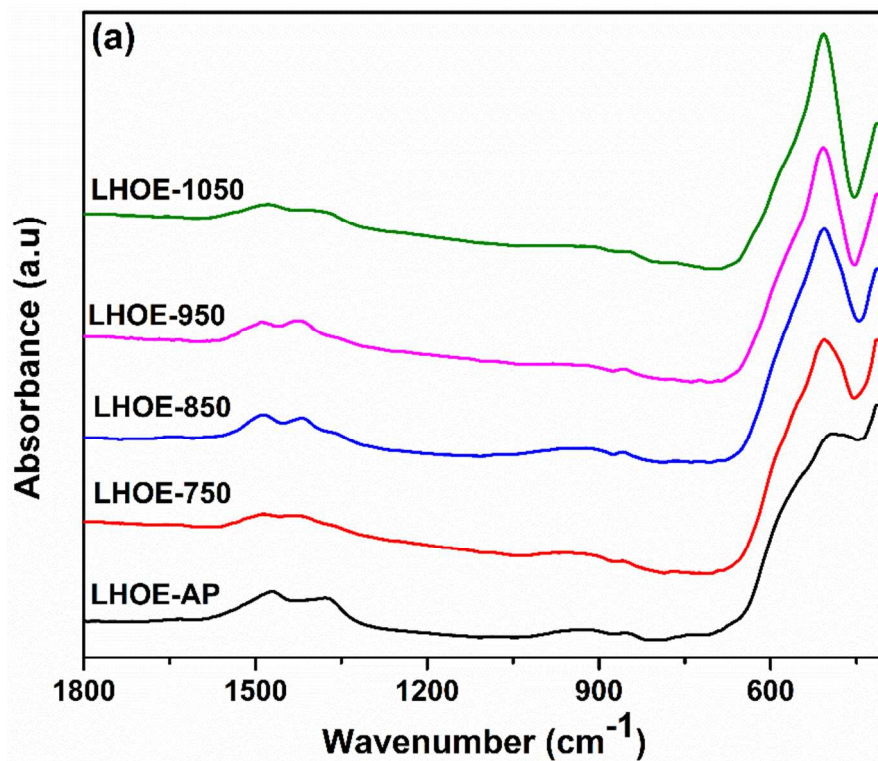


Figure 3. (a) Raman spectra of the $\text{La}_2\text{Hf}_2\text{O}_7:\text{Eu}^{3+}$ NPs annealed at different temperatures. (b) Variation in FWHM of the Raman band as a function of annealing temperature.

3.1.3 FTIR spectroscopy

Wet chemistry route are known to stabilize nanoparticles at low temperature and can effectively control their size, shape, structure and crystallinity. However, it can lead to adsorption of hydroxyl, carbonate and nitrate ions on its surface. These ions are known fluorescence quenchers and can adversely affect the quantum efficiency in case of luminescent materials. Usually, ions such as O-H and N-H with high vibrational frequency provide additional non-radiative pathways and quench the fluorescence from rare earth ions.⁴⁸ Figure 4a shows the FTIR spectra of the $\text{La}_2\text{Hf}_2\text{O}_7:\text{Eu}^{3+}$ NPs originally synthesized and annealed at different temperatures, which show IR absorption bands around 920-940 and around 1385-1450 cm^{-1} . In MSS, NH_4OH is used as a precipitant to precipitate out complex precursor $\text{La}(\text{OH})_3 \cdot 5\% \text{Eu}(\text{OH})_3 \cdot \text{HfO}(\text{OH})_2 \cdot n\text{H}_2\text{O}$. NH_4OH have two very strong absorption bands: one at about 3300–3030 cm^{-1} and another sharper peak at about 1430–1390 cm^{-1} respectively due to the stretching and deformation vibrations of N–H band.⁴⁹ In our samples there are sharp absorption peaks around 1385-1450 cm^{-1} attributed to N-H deformation band.⁵⁰ The other band at 920-940 cm^{-1} is attributed to bending mode of hydroxyl ion²¹ that also seems to recedes a function of annealing temperature. As a function of annealing temperature the intensity decreases (Figure 4b and 4c), which may be responsible for the enhancement in PL emission intensity as a function of annealing temperature till 950°C (Figure 5b) as they are known to quench fluorescence by providing additional pathways for non-radiative transition. The peak at 507 cm^{-1} (ν_1) corresponds to vibration of Hf-O bond.



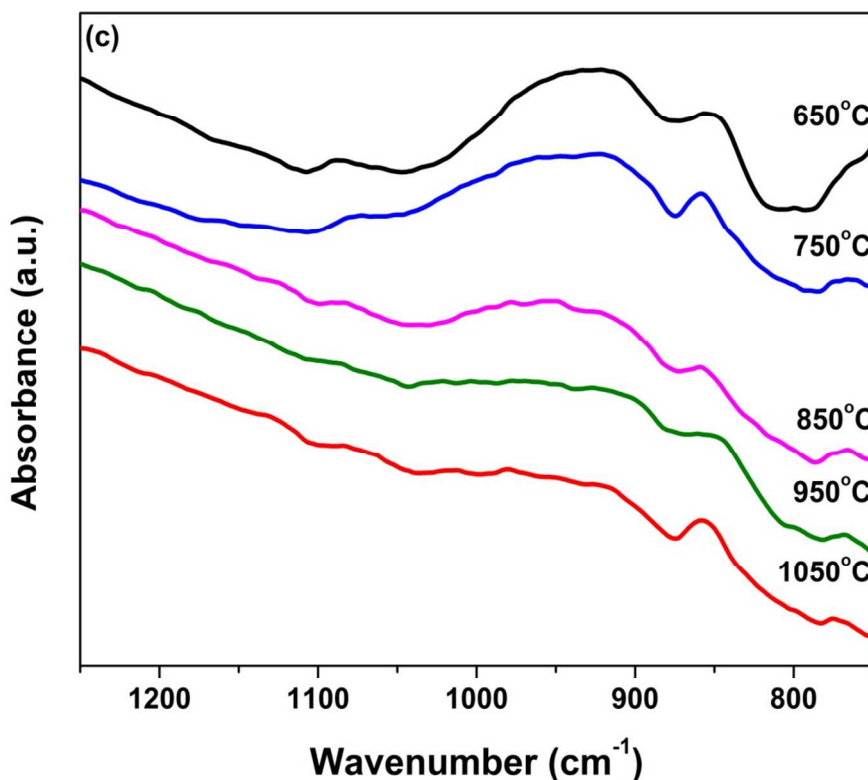


Figure 4. Thermal annealing effect on (a) FTIR spectra and intensity variation of (b) the N-H deformation and (c) the O-H bending IR bands of the $\text{La}_2\text{Hf}_2\text{O}_7:\text{Eu}^{3+}$ NPs.

3.2 Thermal annealing effect on emission characteristics

Figure 5a depicts the emission spectra of the $\text{La}_2\text{Hf}_2\text{O}_7:\text{Eu}^{3+}$ NPs at various annealing temperatures under excitation of the charge transfer band (CTB). The spectra consisted of typical europium emissions at 578, 586, 612, 654 and 708 nm corresponding to $^5\text{D}_0 \rightarrow ^7\text{F}_0$, $^5\text{D}_0 \rightarrow ^7\text{F}_1$, $^5\text{D}_0 \rightarrow ^7\text{F}_2$, $^5\text{D}_0 \rightarrow ^7\text{F}_3$ and $^5\text{D}_0 \rightarrow ^7\text{F}_4$ transitions, respectively. Among these transitions, $^5\text{D}_0 \rightarrow ^7\text{F}_1$ is called magnetic dipole transition (MDT), which is not affected by the crystal/ligand field or any kind of perturbation around europium ion. On the other hand, $^5\text{D}_0 \rightarrow ^7\text{F}_2$ is called as hypersensitive electric dipole moment transition (EDT) is strongly influenced by the crystal or ligand field. $^5\text{D}_0 \rightarrow ^7\text{F}_0$ transition is allowed neither by MDT nor by EDT and is normally seen when the site symmetry around europium ion is very low, normally C_s , C_n or C_{nv} . The presence of this particular transition in the $\text{La}_2\text{Hf}_2\text{O}_7:\text{Eu}^{3+}$ NPs indicated that europium ion is not localized in symmetric environment. This is further supported by high intensity of the EDT compared to the magnetic dipole one. The fact that we could observe the $^5\text{D}_0 \rightarrow ^7\text{F}_0$ forbidden transition and high intensity of EDT compare to MDT indicates that europium ion is localized at distorted LaO_8 scalenohedra.

In fact, the integral ratio of ${}^5D_0 \rightarrow {}^7F_2$ transition (EDT) to ${}^5D_0 \rightarrow {}^7F_1$ (MDT) transition, known as asymmetry ratio (R/O), gives insight on the local site symmetry around europium ion and is highly sensitive to any changes around europium ion. Table 2 tabulates the BET specific surface area, quantum yield, and R/O values of the $\text{La}_2\text{Hf}_2\text{O}_7:\text{Eu}^{3+}$ NPs annealed at various temperatures. It can be seen that the R/O decreases systematically as the annealing temperature is increased and has a value greater than 1.0 for all the samples up to 950°C . This phenomenon indicates that Eu^{3+} ions are located at asymmetric sites with no inversion center in these samples. However, for the sample annealed at 1050°C , the R/O was found to be 0.90 (MDT > EDT) indicating a highly symmetric environment of europium ion with inversion center. The systematic decreases in R/O with annealing temperature is because the extent of distortion around Eu^{3+} ions at LaO_8 or HfO_6 sites decreases at higher annealing temperature. This can also be correlated with the fact that the structure becomes more and more ordered (ideal pyrochlore) as the annealing temperature is increased with the highest degree of cation and anion ordering in the sample annealed at 1050°C , which is supported by Raman spectroscopy (Figure 3). This can be visually observed from the emission spectra wherein the intensity of MDT is higher than that of EDT for the NPs annealed at 1050°C . The systematic decreases in asymmetry ratio as the annealing temperature increases is attributed to increased pyrochlore ordering as is also confirmed using Raman spectroscopy which depicted least ordering in 650°C annealed sample and perfect ordered pyrochlore structure for 1050°C annealed sample.

Another interesting observation, which could be made from Figure 5a, is the unusual emission profile of the sample annealed at 1050°C compared to the others. The spectrum of the sample annealed at 1050°C is different to those obtained on heating up to 950°C in terms of their line shapes. At 1050°C , the intensity of the peak at 590 nm increases and overpower EDT at 612 nm; which indicates that the symmetry around the Eu^{3+} ions is significantly improved in this sample compared with in the samples annealed up to 950°C . It is reported by Nigam et al. in their work on $\text{Y}_2\text{Sn}_2\text{O}_7:\text{Eu}^{3+}$ that AO_8 polyhedra becomes more and more symmetric at higher temperatures due to change in the orientation of oxygen atom around yttrium (or A) site.⁵¹

In case of our $\text{La}_2\text{Hf}_2\text{O}_7:\text{Eu}^{3+}$ NPs, the LaO_8 polyhedron attained more symmetric environment as the temperature is increased and finally at 1050°C the oxygen ions are located in such a way that it has inversion symmetry and MDT increased more than EDT. Another reason is tunneling

of europium ion from distorted LaO_8 scalenohedra to perfect HfO_6 octahedral at 1050°C which is reflected in intense MDT in case of the LHOE-1050 NPs.

It was also observed from Figure 5b that the relative emission intensity of the $\text{La}_2\text{Hf}_2\text{O}_7:\text{Eu}^{3+}$ NPs increases progressively with annealing temperature up to 950°C and then there is slight reduction in emission intensity at 1050°C . To probe this we have measured the specific surface area of the $\text{La}_2\text{Hf}_2\text{O}_7:\text{Eu}^{3+}$ NPs (Table 2). As can be seen, the surface area progressively decreases as the annealing temperature is increased which is attributed to the increase of crystallite size. Surface area is known to drastically influence the PL intensity that are present in abundance in case of NPs. Surface defect in a nanomaterial is related to its surface area. Larger the surface area, more europium ions located near the NPs' surface, and more surface defects which can quench fluorescence. The enhancement in PL emission intensity up to 950°C can be ascribed to decrease in surface area/surface defect, which are known to provide additional pathways for non-radiative transitions.^{41, 52} Another reason is the reduction in N-H and O-H vibrations as a function of annealing temperature as seen from FTIR spectra (Figure 4b). The enhanced PL intensity was attributed to the decrease of N/O related defects by thermal annealing. Huang et al. have observed similar phenomenon in SiN films.⁵³ This is attributed to breaking of N-H/O-H bond at high temperature, which results in reduction of N-H/O-H vibrational intensity in case of our $\text{La}_2\text{Hf}_2\text{O}_7:\text{Eu}^{3+}$ NPs.⁵⁴

Beyond 950°C , the NPs tend to agglomerate to such an extent that it overpowers the effect of surface area and causes scattering of the emitted light and thereby decreasing the observed emission intensity. Therefore, the slight reduction in PL intensity beyond certain crystallite size is attributed to larger crystallite size, which tends to scatter light in particle excitation, leading to decrease in emission intensity.⁵⁵ Table 2 lists the quantum yield values of our $\text{La}_2\text{Hf}_2\text{O}_7:\text{Eu}^{3+}$ NPs annealed at various temperatures. Similar correlation can be found in the quantum yield measurements, wherein the LHOE-950 NPs were found to have the maximum QY of 20.82%.

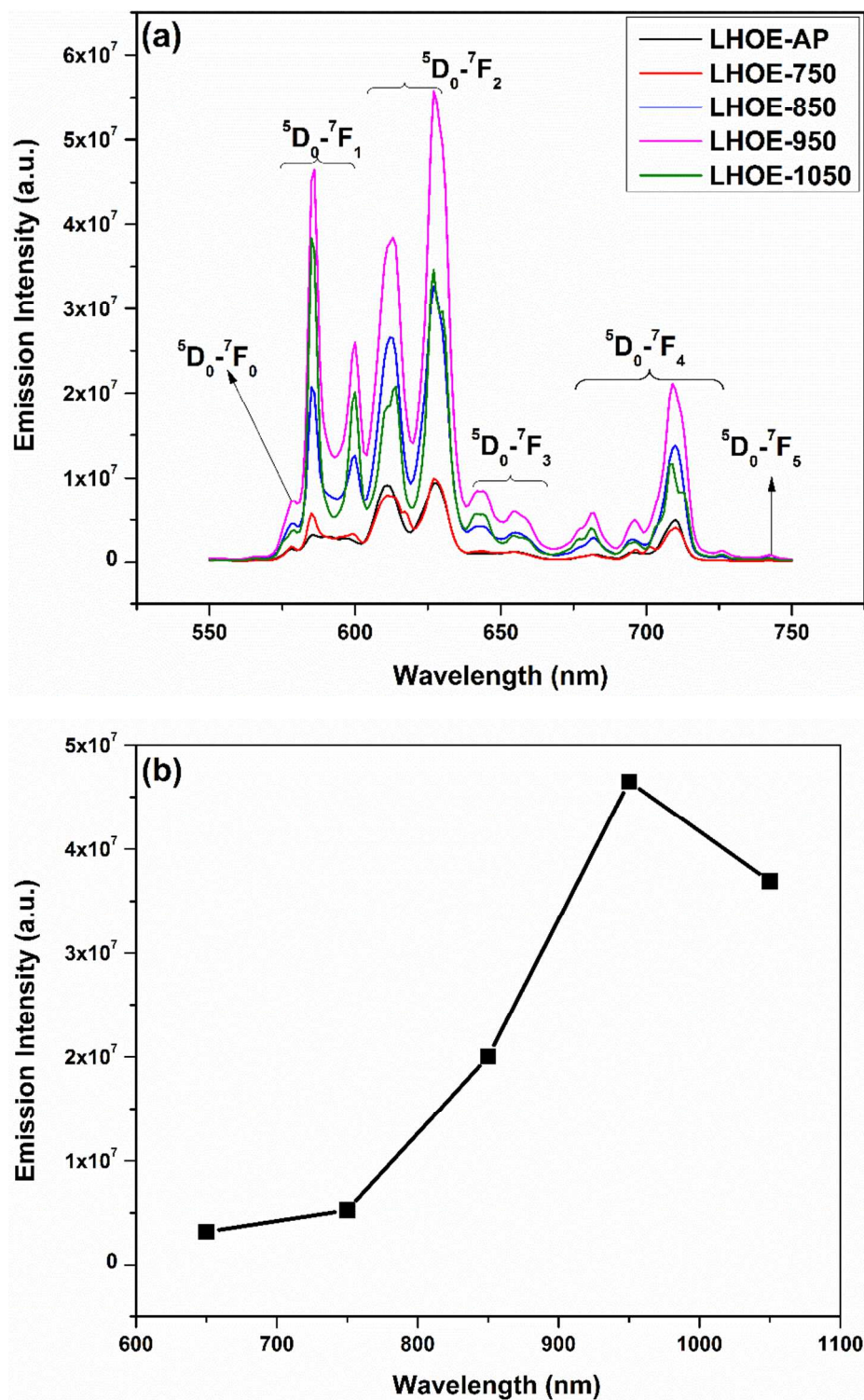


Figure 5. Thermal annealing effect on (a) the emission spectra recorded under excitation with charge transfer state excitation and (b) the variation in emission intensity of ${}^5D_0 \rightarrow {}^7F_1$ transition.

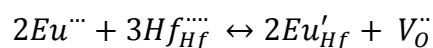
Table 2. BET surface area, quantum yield and asymmetry ratio of the $\text{La}_2\text{Hf}_2\text{O}_7:\text{Eu}^{3+}$ NPs as a function of annealing temperature

Samples	BET surface area (m^2/g)	PL asymmetry ratio	Quantum yield (QY)
LHOE-AP	25.007±0.1802	2.96	16.52
LHOE-750	18.982±0.0838	1.72	18.27
LHOE-850	15.293±0.0570	1.58	19.73
LHOE-950	9.6559±0.0365	1.23	20.82
LHOE-1050	6.8072±0.0296	0.90	18.13

When the lanthanide ion is doped in an inorganic host lattice, the energy levels of the lanthanide ion get split into various sublevels due to the crystal field effect. These sublevels are called as Stark sublevels with maximum number of $(2J + 1)$ (where J is the electronic angular momentum). Based on number of Stark sub-levels seen in the ${}^5\text{D}_0 \rightarrow {}^7\text{F}_J$ transitions of Eu^{3+} ion, we can determine the local symmetry of the Eu^{3+} ion at $\text{La}^{3+}/\text{Hf}^{4+}$ site in $\text{La}_2\text{Hf}_2\text{O}_7$. Among various transitions of Eu^{3+} ion, ${}^5\text{D}_0 \rightarrow {}^7\text{F}_0$, ${}^5\text{D}_0 \rightarrow {}^7\text{F}_1$ (MDT) and ${}^5\text{D}_0 \rightarrow {}^7\text{F}_2$ (EDT) are the most important and informative ones. Other transitions such as ${}^5\text{D}_0 \rightarrow {}^7\text{F}_4$ is not hypersensitive in nature whereas ${}^5\text{D}_0 \rightarrow {}^7\text{F}_3$ is neither allowed by EDT nor MDT. In this case, we have considered the emission pattern of ${}^5\text{D}_0 \rightarrow {}^7\text{F}_0$, ${}^5\text{D}_0 \rightarrow {}^7\text{F}_1$ and ${}^5\text{D}_0 \rightarrow {}^7\text{F}_2$ to calculate the local symmetry of europium ion in $\text{La}_2\text{Hf}_2\text{O}_7$. Figure S4 shows the selective emission range of ${}^5\text{D}_0 \rightarrow {}^7\text{F}_0$, ${}^5\text{D}_0 \rightarrow {}^7\text{F}_1$ and ${}^5\text{D}_0 \rightarrow {}^7\text{F}_2$ of the $\text{La}_2\text{Hf}_2\text{O}_7:\text{Eu}^{3+}$ NPs under various annealing temperatures. As a function of annealing temperature not many changes were seen in the number of stark components for all three transitions.

The substitution of La^{3+} with Eu^{3+} may lead to significant lattice distortion because of distorted nature of LaO_8 scalenohedra in ideal pyrochlore structure. On the other hand, the substitution of perfect Hf^{4+} octahedra site with Eu^{3+} ion may lead to substantial lattice strain not only due to local symmetry, but also due to mismatch between ionic radius and ionic size between Eu^{3+} and Hf^{4+} . Charge compensation in this case will be by creation of positively charge oxygen vacancies (V_{O}) and negatively charged antisite defect (Eu'_{Hf}).

When trivalent europium ion goes to tetravalent hafnium site, charge compensation takes place by formation of oxygen vacancies as indicated below:



Such lattice strain combined with these kinds of defects reduces the original symmetry existing around La and Hf sites in $\text{La}_2\text{Hf}_2\text{O}_7$ which is D_{3d} . From stark splitting patterns shown in Figure S4, one peak for ${}^5\text{D}_0 \rightarrow {}^7\text{F}_0$ transition, two peaks for ${}^5\text{D}_0 \rightarrow {}^7\text{F}_2$ EDT (hypersensitive, $\Delta J = \pm 2$) and two peaks for ${}^5\text{D}_0 \rightarrow {}^7\text{F}_1$ ($\Delta J = \pm 1$) MDT of Eu^{3+} were resolved. According to the branching rules of various point groups reported for europium ion,⁵⁶ it infers that the actual site symmetry of Eu^{3+} in the $\text{La}_2\text{Hf}_2\text{O}_7$ NPs reduces from original D_{3d} to C_6 .

3.3 Thermal annealing effect on PL excitation characteristics

In most of the phosphor materials, Eu^{3+} ion cannot be efficiently excited by near UV light (395 nm) due to its poor molar absorption coefficient ($< 5 \text{ M}^{-1} \text{ cm}^{-1}$)⁵⁷ owing to its forbidden f-f nature of ${}^7\text{F}_0 \rightarrow {}^5\text{L}_6$. To overcome these problems, proper sensitizer ions or host materials must be selected to sensitize Eu^{3+} to obtain ideal and tunable phosphor materials. This particular phosphor material, because of the fact that it has very intense peaks at 395, 465 and 534 nm, ultra-violet (UV), near-UV, UV-blue (UVB), and blue or green laser diodes/ LEDs can act as efficient pumping sources for the red emission from Eu^{3+} ions. Figure 6a shows the excitation spectra of the $\text{La}_2\text{Hf}_2\text{O}_7:\text{Eu}^{3+}$ NPs at various annealing temperatures, and by monitoring the red emission band at 612 nm, corresponding to ${}^5\text{D}_0 \rightarrow {}^7\text{F}_2$ transition of europium ion. The excitation intensity increases monotonously with annealing temperature. There are two main features: (i) broad band in the region of 265-330 nm attributed to oxygen to europium charge transfer band (CTB) and (ii) the fine spectral features from 350-550 nm of the f-f transitions of europium ion. The study of the change in spectral position of CTB in the $\text{La}_2\text{Hf}_2\text{O}_7:\text{Eu}^{3+}$ NPs as a function of annealing temperature (grain size) is very important for proper understanding on the interaction between host and lanthanide ion in nanophosphor. We could also find some variation in broadness as well as position of this band in our nanoparticles. Although there is not perfect correlation in spectral band shift but higher temperature annealed samples (850, 950 and 1050) are blue shifted w.r.t to lower annealed one (650 and 750°C). The lack of perfect correlation can be due to contribution of other transitions in CTB such as $\text{O}^{2-} \rightarrow \text{La}^{3+}$, $\text{O}^{2-} \rightarrow \text{Hf}^{4+}$, and $\text{Hf}^{4+} \rightarrow \text{Eu}^{3+}$. The charge transfer energy for large sized nanophosphor is more than that for smaller one. Charge transfer process is strongly influenced by Eu-O bond energy. In smaller sized NPs higher surface to volume ratio destabilizes Oxygen ion and therefore Eu-O has less bond energy.⁵⁸ If Eu-O bond energy decreases, the bond weakens and it becomes easier for oxygen to transfer

electron to europium ion and therefore charge transfer energy decreases and there is red shift in smaller size grains.⁵⁹ Another interesting thing is the narrowing of CTB as the annealing temperature increases. This may be because of predominating contribution of only one kind of charge transfer at higher temperature, i.e. $O^{2-} \rightarrow Eu^{3+}$ and the other transitions mentioned above has minimal contribution. Emission characteristics of the $La_2Hf_2O_7:Eu^{3+}$ NPs under various excitation wavelength are shown in Figure 6b. All spectra display characteristic peaks of europium ion. Red emission output under excitation with near UV or Blue LEDs are very poor relative to excitation with La Porte allowed charge transfer band (CTB). However, all commercial application of phosphor materials needs it to be excited under near UV (~395 nm) or blue light (~464 nm). The $La_2Hf_2O_7:Eu^{3+}$ NPs can be easily excited using UV, Violet, Blue and green LEDs and are highly successful in giving an intense red ${}^5D_0 \rightarrow {}^7F_2$ emission at 616 nm. Such materials can be used for phosphor converted white LEDs and can be explored for other applications such as bioimaging and water disinfection.

The colorimetric performance of synthesized nanoparticles at various excitation wavelength were analyzed based on CIE index diagram shown in Figure S5. The emission results obtained after corrections for the $La_2Hf_2O_7:Eu^{3+}$ NPs at room temperature is shown in the CIE diagram, and it is seen that our samples give red-orange emission at all the excitation wavelength ranging from mid UV, near UV, to blue and green light. The CIE coordinates of the samples does not changed much with excitation wavelength, so the exact coordinates (x, y) are given in Table 3. We can see from the CIE index diagram that the doped pyrochlore NPs give stable red color emission with high color purity, which is highly favorable for light emitting diodes applications.⁶⁰ Table 3 also presents the correlated color temperature (CCT) of the $La_2Hf_2O_7:Eu^{3+}$ NPs under various excitation wavelength that was calculated based on equation (1) reported by McCamy.⁶¹

$$T = -437n^3 + 3601n^2 - 6861n + 5514.31 \quad (1)$$

$$\text{where } n = \frac{x - 0.332}{y - 0.186}$$

In practice, the more the CCT, the lighter in nature the emitted light color. We can observe that although some coordinates are overlapped (Figure S5) the color temperatures are distinct. It is believed that the CIE coordinate and CCT rare very important photophysical parameter which could be highly useful in designing materials for optical emitters or other luminescent devices.⁶⁰

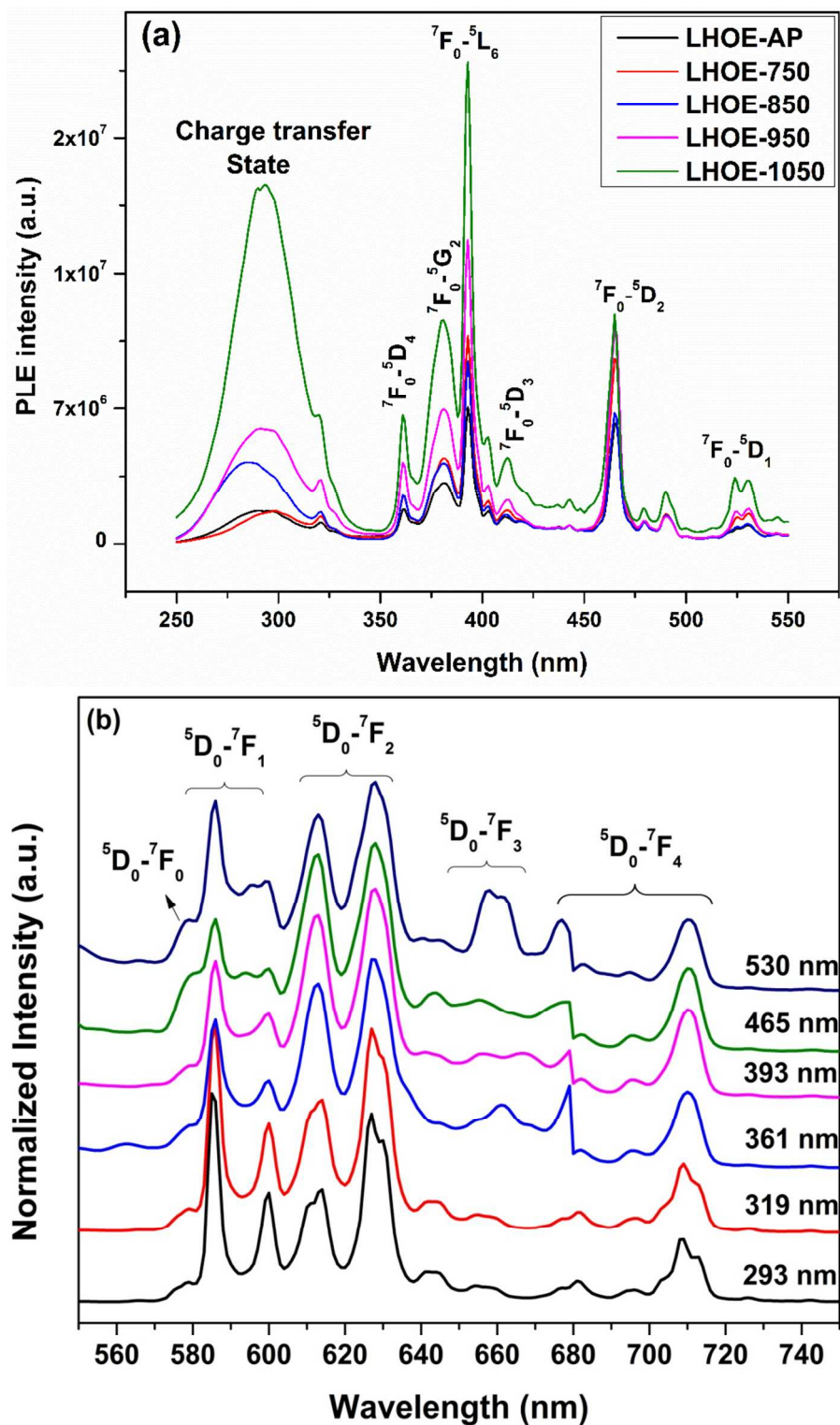


Figure 6. (a) Thermal annealing effect on excitation spectra of the $\text{La}_2\text{Hf}_2\text{O}_7:\text{Eu}^{3+}$ NPs. (b) Emission spectra of the LHOE-1050 NPs excited by various wavelengths.

Table 4. CIE chromaticity coordinates and the CCT of the LHOE-1050 NPs excited at various wavelengths

Excitation wavelength (nm)	CIE chromaticity coordinates (x, y)	Color temperature (K)
293	(0.632, 0.367)	2045
319	(0.632, 0.367)	2045
361	(0.622, 0.377)	1869
393	(0.630, 0.389)	2005
465	(0.616, 0.382)	1804
530	(0.606, 0.392)	1731

3.4 Thermal annealing effect on luminescence lifetime

The luminescence decay profiles of the $\text{La}_2\text{Hf}_2\text{O}_7:\text{Eu}^{3+}$ NPs annealed at different temperatures are shown in Figure S6 under excitation of 293 nm corresponding to $^5\text{D}_0 \rightarrow ^7\text{F}_2$ emission at 612 nm. The NPs annealed up to 850°C displayed two different slopes with biexponential decay profile that suggests two different lifetimes of Eu^{3+} ion in these $\text{La}_2\text{Hf}_2\text{O}_7:\text{Eu}^{3+}$ NPs. The biexponential decay can be due to various reasons such as host sensitized energy transfer, non-homogenous distribution of europium ion in lanthanum hafnate lattice and presence of defects. The lifetime values of Eu^{3+} ion were determined using biexponential decay profile using the second order function (Eq. 2):

$$I(t) = B_1 \exp(-t/\tau_1) + B_2 \exp(-t/\tau_2) \quad (2)$$

where $I(t)$ is the PL intensity at time t , B_1 and B_2 are residual weighting factors of each lifetime, t is time of measurements, τ_1 and τ_2 are the lifetime values of the first and the second components, respectively.

On the other hand, the samples annealed at 950 and 1050°C showed monoexponential decay profile with only one lifetime value. The reason for such anomalous behavior can be ascribed to the distribution of europium ion at both LaO_8 and HfO_6 sites when samples were annealed in temperature range of 650-850°C. Assuming the concept of Laporte's selection rule which is valid for system having center of symmetry, the higher lifetime in the range of 2.5-3.3 ms (Eu_L) is attributed to Eu^{3+} ion localized at more symmetric Hf^{4+} site in ideal pyrochlore structure though compensation by oxygen vacancies is needed in this case. The lower lifetime value in the range

of 930-1000 μs (Eu_S) is attributed to europium ion sitting at distorted La^{3+} site. On the other hand, when the sample is exposed to higher annealing temperatures of 950 and 1050°C, all europium ions sitting at low symmetric La-site tunnel to highly symmetric Hf^{4+} site, which is the reason for their monoexponential behavior with lifetime in the order of 2.6/3.0 ms.

The individual lifetime, with their magnitude along with the average lifetime is tabulated in Table 4. The trends in the average lifetime as a function of annealing temperature is similar to what has been found for emission intensity. This is again attributed to the decrease in non-radiative relaxation, which arose from surface defect of the NPs. The other reason is similar to what has been discussed earlier too that as the annealing temperature increase there is a decrease in quenching of the Eu^{3+} luminescence by the vibrations of the impurities such as $-\text{OH}$, $-\text{NH}$, and $-\text{C-H}$. The quantum yield of the LHOE-950 NPs is found to be approximately 21%.

TRES was carried out to elucidate the emission spectra of two different kinds of europium ions Eu_L and Eu_S (Figure S7). The two europium ions differ drastically in terms of asymmetry ratio. For Eu_L (long lived) asymmetry ratio is 1.05 indicating its presence in highly symmetric Hf^{4+} site with inversion symmetry. For Eu_S (short lived), EDT is much more intense than MDT (asymmetry ratio = 5.0) indicating their presence in relatively asymmetric La^{3+} site without inversion symmetry.

Table 4. Luminescence lifetime for the $\text{La}_2\text{Hf}_2\text{O}_7:\text{Eu}^{3+}$ NPs annealed at different temperatures

Samples	τ_1 (ms)	τ_2 (ms)	Population		τ_{avg} (ms)
			τ_1 (%)	τ_2 (%)	
LHOE-AP	0.936	2.56	26	74	2.14
LHOE-750	1	2.73	30	70	2.34
LHOE-850	1	3.23	25	75	2.71
LHOE-950	3.02				3.02
LHOE-1050	2.60				2.60

3.5 Site Specific luminescence in LHOE-1050 NPs

Figures 7a and 7b show the emission spectra of the LHOE-1050 NPs excited at $\lambda_{\text{ex}} = 293$ nm (charge transfer band) and 393 nm (f-f band), respectively. The spectra consist of various emission peaks in the range of 565-745 nm corresponding to the unique spectral feature of

trivalent europium ion in solids arising from ${}^5D_0 \rightarrow {}^7F_J$ ($J = 0-5$) transitions. The interesting observation that could be seen is the difference in the emission features under CTB and f-f band excitation. Such behavior is attributed to localization of europium ion in two different local environments in a single host matrix.^{23, 28, 62} As discussed earlier, the orange emission around 592 nm of Eu^{3+} is governed by magnetic dipole transition (MDT) ${}^5D_0 \rightarrow {}^7F_1$ and is not affected much by the local site symmetry around europium ions because they are parity-allowed in nature. On the other hand the red emission around 612 nm governed by electric dipole transition (EDT) ${}^5D_0 \rightarrow {}^7F_2$ ($\Delta J = \pm 2$) being hypersensitive in nature is strongly affected by the local site symmetry of Eu^{3+} ions.

Upon excitation with 293 nm (CTB), the emission spectrum is governed by strong MDT relative to EDT along with presence of other transitions such as ${}^5D_0 \rightarrow {}^7F_3$ (654 nm) and ${}^5D_0 \rightarrow {}^7F_4$ (708 nm). No host emission could be seen indicating efficient host sensitized energy transfer in our $\text{La}_2\text{Hf}_2\text{O}_7:\text{Eu}^{3+}$ NPs. On the other hand, upon excitation at 393 nm (f-f band of europium ion), ${}^5D_0 \rightarrow {}^7F_2$ transition at 612 nm (EDT) is more intense compared to ${}^5D_0 \rightarrow {}^7F_1$ line at 592 nm (MDT). The distinct differences in the emission spectra of the $\text{La}_2\text{Hf}_2\text{O}_7:\text{Eu}^{3+}$ NPs under different excitation wavelengths (293 and 393 nm) suggest the possibility of Eu^{3+} ions occupying two different local sites in the $\text{La}_2\text{Hf}_2\text{O}_7$ NPs.

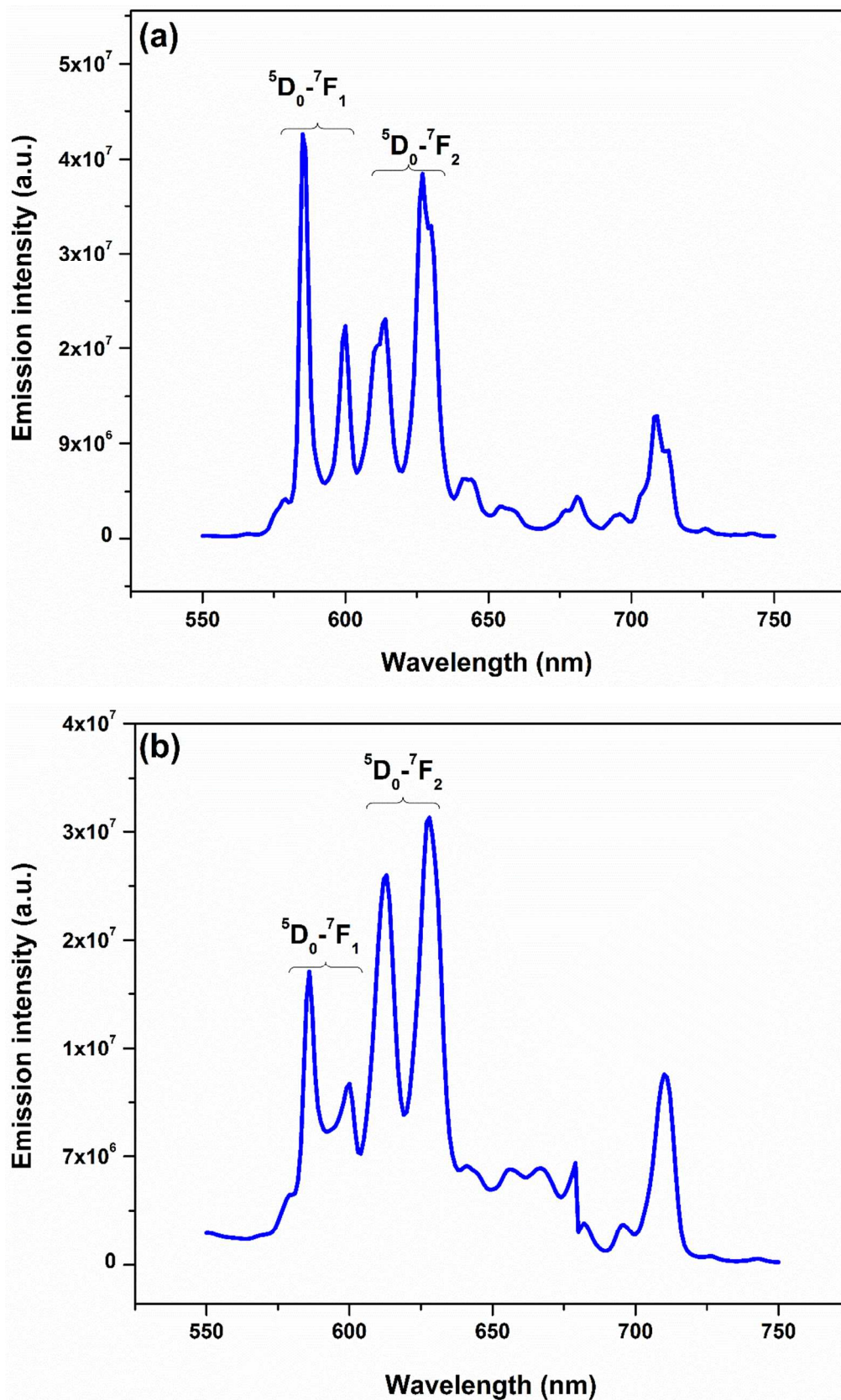
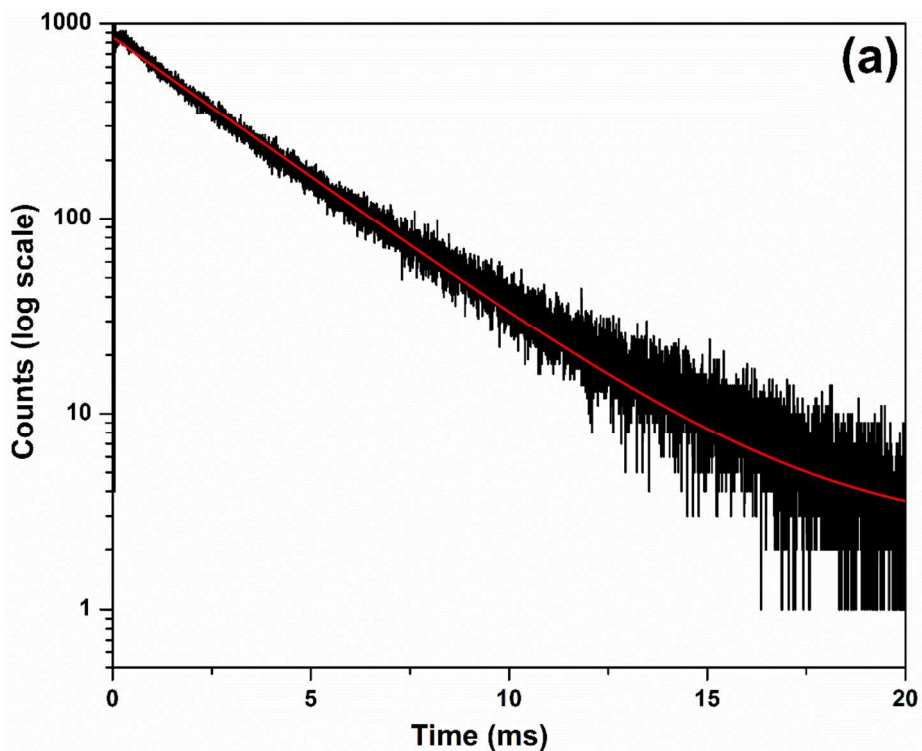


Figure 7. Emission spectra of the LHOE-1050 NPs with (a) 293 nm and (b) 393 nm excitations.

The possibility of Eu^{3+} ions occupying two different local sites in the $\text{La}_2\text{Hf}_2\text{O}_7$ NPs is also corroborated by lifetime measurement data (Figure 8). After proper exponential fitting, we could find a single lifetime under 293 nm excitation (2.61 ms) whereas two lifetimes under 393 nm excitation (1.16 and 2.71 ms). This suggests that pumping the $\text{La}_2\text{Hf}_2\text{O}_7:\text{Eu}^{3+}$ NPs with excitation energy corresponding to 293 nm specifically excite the europium ion with longer lifetime of 2.6 ms, which is the one sitting at Hf^{4+} site. On the other hand, pumping them at 393 nm can excite the europium ion with lifetimes of 1.16 (Eu_S) and 2.71 ms (Eu_L) corresponding to the ones sitting at La^{3+} and Hf^{4+} sites. Based on emission and lifetime studies, we could find that there were two types of europium ions [1.16 ms (T_1) and 2.6 ms (T_2)]. Charge transfer band (293 nm) excites Eu_L selectively whereas f-f band (393 nm) excites both Eu_S (34 %) and Eu_L (66 %).



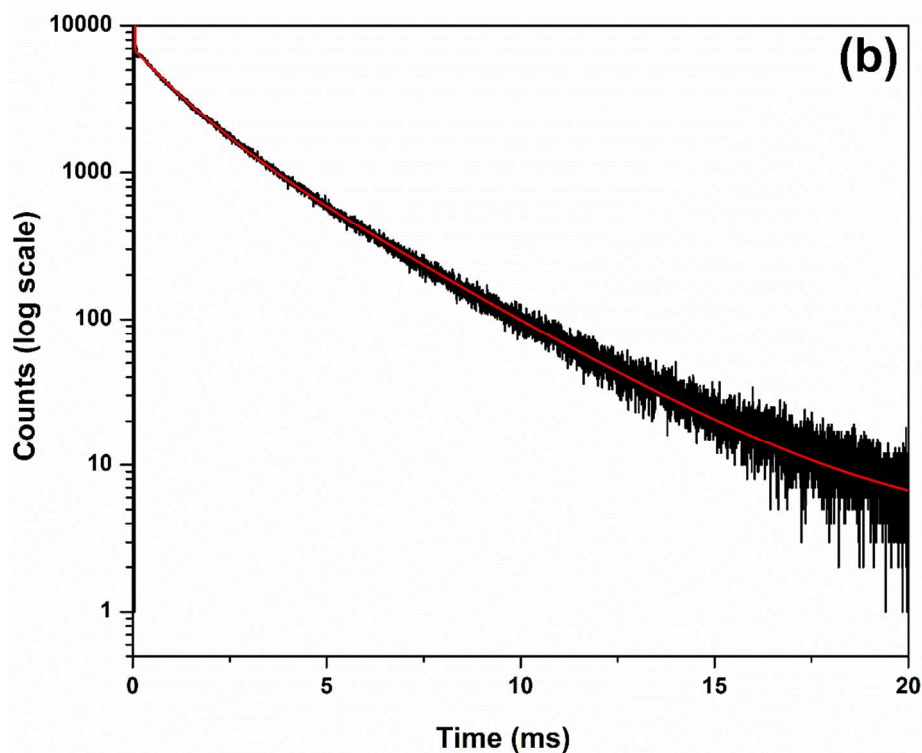


Figure 8. Luminescence decay profile of the LHOE-1050 NPs under (a) $\lambda_{\text{ex}} = 293$ nm and $\lambda_{\text{em}} = 612$ nm and (b) $\lambda_{\text{ex}} = 393$ nm and $\lambda_{\text{em}} = 612$ nm. Black curves are the experimental data whereas red ones are the fittings.

3.6 Thermal annealing effect on X-ray excited optical luminescence

The X-ray excited luminescence (XEL) spectra of the $\text{La}_2\text{Hf}_2\text{O}_7:\text{Eu}^{3+}$ NPs annealed at various temperatures (Figure 9) depict the typical feature of europium ion in low symmetric environment. The higher intensity of EDT than MDT reflects the fact of europium occupying distorted LaO_8 scalenohedra. At any annealing temperature, the MDT at 592 nm is weaker than EDT transition (612) which is different from UV excited luminescence. In UV excited PL in case of the LHOE-1050 NPs we could see intense MDT compared to EDT. However, the trend in emission intensity as function of annealing temperature is slightly different from that observed in UV/NUV excitation. Here there is monotonous variation in emission intensity as a function of annealing temperature and the LHOE-1050 NPs have the maximum emission intensity. The difference in the optimum annealing temperature of XEL and PL ($\lambda_{\text{ex}} = 293$ nm) is due to the difference in the excitation mechanism. Another interesting feature, which could be seen from XEL spectra, is the change in the asymmetry ratio (R/O) as a function of annealing temperature

(Table 5). In UV excited PL, there was a decrease of R/O as a function of annealing temperature. However, here in XEL, we are seeing a reverse trend, i.e. R/O increases with the increase of annealing temperature. In XEL, high-energy sources, such as X-ray, which is much more energetic than UV light, generate a large amount of free charge carriers or excitons (e^-h^+) in the $\text{La}_2\text{Hf}_2\text{O}_7$ lattice due to the photoelectric effect. These free charge carriers or excitons (e^-h^+) with the absorbed energy are transported via the crystal lattice and get trapped by activator centers (europium ions in this case) that leads to radiative recombination and emission of light. This suggests that thermal effect on irradiation with X-ray leads to more distortion/randomization in $\text{La}_2\text{Hf}_2\text{O}_7$ lattice at higher annealing temperatures. It is reported that excitons generated by X-ray excitation are highly sensitive to adsorbed surface groups, defects, and defect-like features.⁶³ In this case, a decrease in surface defect (with increase in annealing temperature) leads to more randomization in excitons and charge carriers.

Another interesting feature that could be seen in the inset of the XEL spectra is the presence of small and broad emission peak around 550 nm. This emission band can be ascribed to the typical $4f^65d^1 \rightarrow 4f^7$ transitions from divalent europium ion. This suggest initiation of reduction of Eu^{3+} to Eu^{2+} on X-ray irradiation. We can confirm it by increasing the dose of X-ray beam to see the change in $[\text{Eu}^{2+}]/[\text{Eu}^{3+}]$ emission output. Such phenomenon has also been observed in $\text{CaAl}_2\text{O}_4:\text{Eu}^{3+}$.⁶⁴

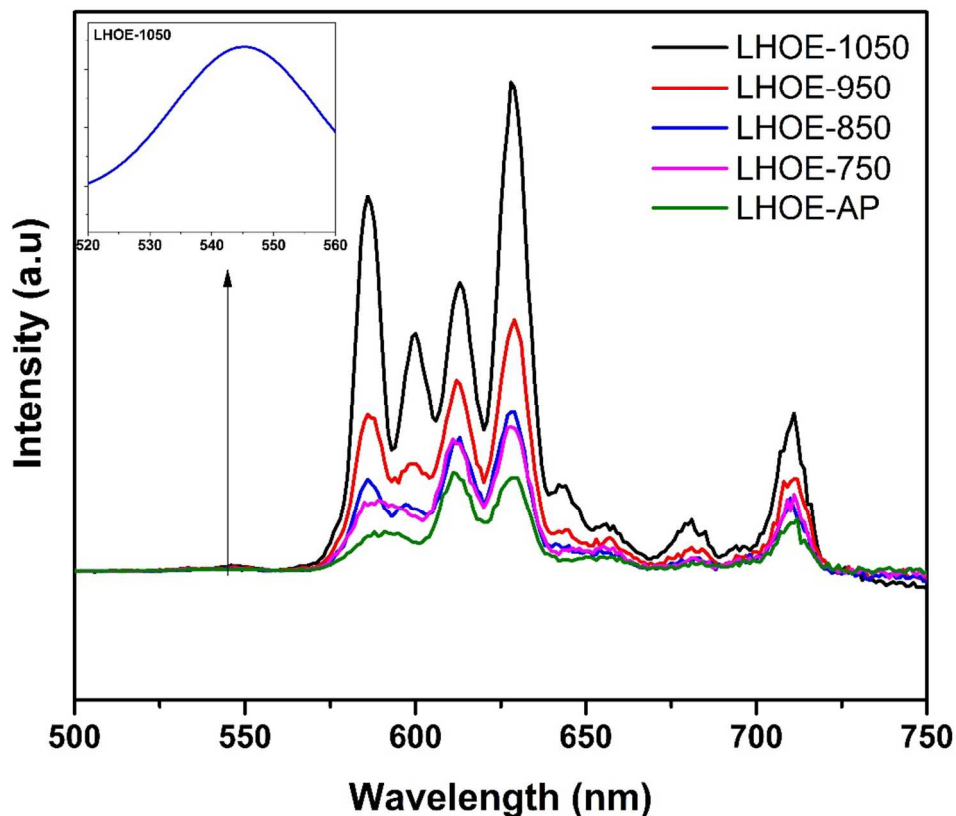


Figure 9. (a) X-ray excited emission spectra of the $\text{La}_2\text{Hf}_2\text{O}_7:\text{Eu}^{3+}$ NPs annealed at different temperatures. Inset shows the XEL spectra from 520-560 nm for 1050°C annealed sample.

Table 5. Asymmetry ratio of the $\text{La}_2\text{Hf}_2\text{O}_7:\text{Eu}^{3+}$ NPs annealed at various temperatures derived from X-ray excited luminescence

Sample	Asymmetry Ratio (XEL)	Asymmetry Ratio (UVEL)
LHOE-AP	1.23	2.96
LHOE-750	1.54	1.72
LHOE-850	1.80	1.58
LHOE-950	2.08	1.23
LHOE-1050	2.78	0.90

3.7 Judd-Ofelt analysis

Judd-Ofelt (J-O) analysis is a very powerful method for evaluating optical properties of Eu^{3+} ion including radiative and non-radiative transition rates, J-O parameters, branching ratios, and quantum efficiency, etc. The mathematical calculations required for such analyses is described extensively elsewhere.²⁴ J-O intensity parameters, in terms of Ω_λ ($\lambda = 2, 4, 6$), are very important to give highly beneficial information for the performance of laser and luminescent materials. Ω_2 gives information about short-range effect such as Eu-O covalency and polarizability whereas Ω_4 is highly informative about long-range effects such as viscosity and rigidity. J-O parameters and other photophysical properties of the $\text{La}_2\text{Hf}_2\text{O}_7:\text{Eu}^{3+}$ NPs annealed at different temperatures are listed in Table 6.

Three main optical observations can be corroborated with these results. (i) From the emission spectra, we found maximum emission intensity the LHOE-950 NPs. This is mainly due to very low non-radiative transition rate (A_{NR}) which is attributed to low surface defects and low NH and OH vibration. (ii) It can also be seen from Table 7 that Ω_2 value is maximum for the LHOE-AP NPs and minimum for the LHOE-1050 NPs. This is also reflected in asymmetry ratio values. This is an indication that the extent of asymmetric environment around europium ions is maximum in the LHOE-AP NPs and minimum in the LHOE-1050 NPs. This is clearly observed in intense MDT than EDT in emission spectra of the LHOE-1050 sample. (iii) Moreover, the J-O parameter shows that $\Omega_2 > \Omega_4$ for the LHOE-950 NPs, which is related to high asymmetry of the Eu^{3+} surrounding environment whereas $\Omega_4 > \Omega_2$ for the LHOE-1050 NPs. This is an interesting observation that suggests that annealing the NPs to 1050°C enhances the symmetry around europium ion to an extent that the orange emission starts predominating the red one.

Table 6. Radiative and non-radiative decay rates, Judd–Ofelt intensity parameters, and branching ratios of the $\text{La}_2\text{Hf}_2\text{O}_7:\text{Eu}^{3+}$ NPs annealed at various temperatures

Sample	$A_{\text{R}} (\text{s}^{-1})$	$A_{\text{NR}} (\text{s}^{-1})$	$\Omega_2 (\times 10^{-20})$	$\Omega_4 (\times 10^{-20})$	$\beta_1 (\%)$	$\beta_2 (\%)$	$\beta_4 (\%)$
LHOE-AP	320	146.84	2.37	1.6	15.6	59.4	20
LHOE-750	267	160.51	1.93	1.24	18.7	58	18.5
LHOE-850	250	119.33	1.82	1.1	20	58.5	17.6
LHOE-950	213	117.79	1.47	0.95	23.4	55.1	17.8
LHOE-1050	183	201.61	1.18	0.79	27.3	51.9	17.4

4. Conclusion

In this work, we have successfully synthesized $\text{La}_2\text{Hf}_2\text{O}_7:\text{Eu}^{3+}$ NPs using a MSS method. The synthesized NPs were subjected to annealing up to 1050°C . There is a progressive increase of the crystalline size and decrease in the surface area with increasing annealing temperature. As a function of annealing temperature ($650\rightarrow 1050^\circ\text{C}$), the PL quantum yield and emission intensity increases progressively up to 950°C and then a slight reduction at 1050°C . This phenomenon has been attributed to decrease in surface defects and -OH and -NH vibrations as function of annealing temperature. Additionally, local symmetry around europium ions is found to increase monotonically as a function of annealing temperature and complete symmetric environment around europium ions was observed at the highest annealing temperature of 1050°C . This is correlated Raman spectra that suggest the $\text{La}_2\text{Hf}_2\text{O}_7$ structure becoming more and more ordered (ideal pyrochlore) with increasing annealing temperature. The highest degree of cation and anion ordering in the $\text{La}_2\text{Hf}_2\text{O}_7:\text{Eu}^{3+}$ NPs is achieved after annealed at 1050°C . The sample annealed at 1050°C displayed site-specific luminescence wherein mid-UV excitation leads to excitation of europium ions sitting at Hf^{4+} site and displayed intense orange emission compared to red emission. On the other hand, excitation with near UV at 393 nm excites both Eu^{3+} at La^{3+} site and Hf^{4+} site and displayed intense red emission compared to orange one. Such studies can be useful in designing need based orange or red phosphors. XEL output was found to be the best for the sample annealed at 1050°C . In all samples, europium ions were in very low symmetry environment. The synthesized materials shows difference emission characteristics in terms of asymmetry and emission output under excitation with highly energetic X-ray beam, which was attributed to different emission mechanisms of the NPs under UV and X-ray excitations. The present study highlights the importance of thermal annealing on designing novel pyrochlore based materials for optoelectronics and scintillators.

Acknowledgement

The authors thank the financial support by the National Science Foundation under CHE (award #1710160) and DMR (grant #1523577) and the USDA National Institute of Food and Agriculture (award #2015-38422-24059). The Department of Chemistry at the University of Texas Rio Grande Valley is grateful for the generous support provided by a Departmental Grant from the Robert A. Welch Foundation (Grant No. BX-0048). SKG thanks the United States-India

Education Foundation (USIEF) and the Institute of International Education (IIE) for his Fulbright Nehru Postdoctoral Fellowship (award# 2268/FNPDR/2017).

References

1. Cho, U.; Riordan, D. P.; Ciepla, P.; Kocherlakota, K. S.; Chen, J. K.; Harbury, P. B., Ultrasensitive optical imaging with lanthanide lumiphores. *Nature chemical biology* **2018**, *14*, 15.
2. Mehlenbacher, R. D.; Kolbl, R.; Lay, A.; Dionne, J. A., Nanomaterials for in vivo imaging of mechanical forces and electrical fields. *Nature Reviews Materials* **2017**, *3*, 17080.
3. Kim, Y. H.; Arunkumar, P.; Kim, B. Y.; Unithrattil, S.; Kim, E.; Moon, S.-H.; Hyun, J. Y.; Kim, K. H.; Lee, D.; Lee, J.-S., A zero-thermal-quenching phosphor. *Nature materials* **2017**, *16*, 543.
4. Han, S.; Qin, X.; An, Z.; Zhu, Y.; Liang, L.; Han, Y.; Huang, W.; Liu, X., Multicolour synthesis in lanthanide-doped nanocrystals through cation exchange in water. *Nature Communications* **2016**, *7*.
5. Zhou, Y.; Han, S. T.; Chen, X.; Wang, F.; Tang, Y. B.; Roy, V. A. L., An upconverted photonic nonvolatile memory. *Nature Communications* **2014**, *5*.
6. Kumar, V.; Ntwaeaborwa, O. M.; Soga, T.; Dutta, V.; Swart, H. C., Rare Earth Doped Zinc Oxide Nanophosphor Powder: A Future Material for Solid State Lighting and Solar Cells. *ACS Photonics* **2017**, *4*, 2613-2637.
7. Sreena, T.; Rao, P. P.; Francis, T. L.; Raj, A. K.; Babu, P. S., Structural and photoluminescence properties of stannate based displaced pyrochlore-type red phosphors: $\text{Ca}_{3-x}\text{Sn}_3\text{Nb}_2\text{O}_{14}:x\text{Eu}^{3+}$. *Dalton Transactions* **2015**, *44*, 8718-8728.
8. Medić, M.; Antić, Ž.; Đorđević, V.; Ahrenkiel, P. S.; Marinović-Cincović, M.; Dramićanin, M. D., Effect of annealing on luminescence of Eu^{3+} - and Sm^{3+} -doped Mg_2TiO_4 nanoparticles. *Journal of Luminescence* **2016**, *170*, 679-685.
9. Meltzer, R.; Feofilov, S.; Tissue, B.; Yuan, H., Dependence of fluorescence lifetimes of $\text{Y}_2\text{O}_3:\text{Eu}^{3+}$ nanoparticles on the surrounding medium. *Physical Review B* **1999**, *60*, R14012.
10. Gupta, S. K.; Ghosh, P.; Reghukumar, C.; Pathak, N.; Kadam, R., Experimental and theoretical approach to account for green luminescence from $\text{Gd}_2\text{Zr}_2\text{O}_7$ pyrochlore: exploring the site occupancy and origin of host-dopant energy transfer in $\text{Gd}_2\text{Zr}_2\text{O}_7:\text{Eu}^{3+}$. *RSC Advances* **2016**, *6*, 44908-44920.
11. Gupta, S. K.; Reghukumar, C.; Kadam, R., Eu^{3+} local site analysis and emission characteristics of novel $\text{Nd}_2\text{Zr}_2\text{O}_7:\text{Eu}$ phosphor: insight into the effect of europium concentration on its photoluminescence properties. *RSC Advances* **2016**, *6*, 53614-53624.
12. Gupta, S. K.; Reghukumar, C.; Sudarshan, K.; Ghosh, P. S.; Pathak, N.; Kadam, R. M., Orange-red emitting $\text{Gd}_2\text{Zr}_2\text{O}_7:\text{Sm}^{3+}$: Structure-property correlation, optical properties and defect spectroscopy. *Journal of Physics and Chemistry of Solids* **2018**, *116*, 360-366.
13. Pokhrel, M.; Wahid, K.; Mao, Y., Systematic studies on $\text{RE}_2\text{Hf}_2\text{O}_7:5\%\text{Eu}^{3+}$ (RE = Y, La, Pr, Gd, Er, and Lu) nanoparticles: effects of the A-site RE^{3+} cation and calcination on structure and photoluminescence. *The Journal of Physical Chemistry C* **2016**, *120*, 14828-14839.
14. Pokhrel, M.; Alcoutlabi, M.; Mao, Y., Optical and X-ray induced luminescence from Eu^{3+} doped $\text{La}_2\text{Zr}_2\text{O}_7$ nanoparticles. *Journal of Alloys and Compounds* **2017**, *693*, 719-729.

15. Wahid, K.; Pokhrel, M.; Mao, Y., Structural, photoluminescence and radioluminescence properties of Eu^{3+} doped $\text{La}_2\text{Hf}_2\text{O}_7$ nanoparticles. *Journal of Solid State Chemistry* **2017**, *245*, 89-97.
16. Richardson, R. P. The thermoresponsive behaviour of selected rare-earth hafnate, zirconate, and titanate compounds. 2016.
17. Vorozhtcov, V. A.; Stolyarova, V. L.; Lopatin, S. I.; Simonenko, E. P.; Simonenko, N. P.; Sakharov, K. A.; Sevastyanov, V. G.; Kuznetsov, N. T., Vaporization and thermodynamic properties of lanthanum hafnate. *Journal of Alloys and Compounds* **2018**, *735*, 2348-2355.
18. Clarke, D. R.; Phillpot, S. R., Thermal barrier coating materials. *Materials Today* **2005**, *8* (6), 22-29.
19. Chaudhry, A.; Canning, A.; Boutchko, R.; Weber, M.; Grønbech-Jensen, N.; Derenzo, S., First-principles studies of Ce-doped $\text{RE}_2\text{M}_2\text{O}_7$ (RE = Y, La; M = Ti, Zr, Hf): A class of nonscintillators. *Journal of Applied Physics* **2011**, *109*, 083708.
20. Ji, Y.-M.; Jiang, D.-y.; Shi, J.-l., Preparation and spectroscopic properties of $\text{La}_2\text{Hf}_2\text{O}_7/\text{Tb}$. *Materials Letters* **2005**, *59*, 868-871.
21. Pokhrel, M.; Burger, A.; Groza, M.; Mao, Y., Enhance the photoluminescence and radioluminescence of $\text{La}_2\text{Zr}_2\text{O}_7:\text{Eu}^{3+}$ core nanoparticles by coating with a thin Y_2O_3 shell. *Optical Materials* **2017**, *68*, 35-41.
22. Gupta, S. K.; Sudarshan, K.; Yadav, A. K.; Gupta, R.; Bhattacharyya, D.; Jha, S. N.; Kadam, R. M., Deciphering the Role of Charge Compensator in Optical Properties of $\text{SrWO}_4:\text{Eu}^{3+}$: A (A = Li^+ , Na^+ , K^+): Spectroscopic Insight Using Photoluminescence, Positron Annihilation, and X-ray Absorption. *Inorganic chemistry* **2018**, *57*, 821-832.
23. Gupta, S. K.; Ghosh, P. S.; Yadav, A. K.; Pathak, N.; Arya, A.; Jha, S. N.; Bhattacharyya, D.; Kadam, R. M., Luminescence properties of $\text{SrZrO}_3/\text{Tb}^{3+}$ perovskite: host-dopant energy-transfer dynamics and local structure of Tb^{3+} . *Inorganic chemistry* **2016**, *55* (4), 1728-1740.
24. Gupta, S. K.; Mohapatra, M.; Godbole, S.; Natarajan, V., On the unusual photoluminescence of Eu^{3+} in $\alpha\text{-Zn}_2\text{P}_2\text{O}_7$: a time resolved emission spectrometric and Judd–Ofelt study. *RSC Advances* **2013**, *3* (43), 20046-20053.
25. Mani, R.; Jiang, H.; Gupta, S. K.; Li, Z.; Duan, X., Role of Synthesis Method on Luminescence Properties of Europium (II, III) Ions in $\beta\text{-Ca}_2\text{SiO}_4$: Probing Local Site and Structure. *Inorganic Chemistry* **2018**, *57*, 935-950.
26. Gupta, S. K.; Ghosh, P. S.; Yadav, A. K.; Pathak, N.; Arya, A.; Jha, S. N.; Bhattacharyya, D.; Kadam, R. M., Luminescence properties of $\text{SrZrO}_3/\text{Tb}^{3+}$ perovskite: host-dopant energy-transfer dynamics and local structure of Tb^{3+} . *Inorganic chemistry* **2016**, *55*, 1728-1740.
27. Gupta, S. K.; Sahu, M.; Ghosh, P.; Tyagi, D.; Saxena, M.; Kadam, R., Energy transfer dynamics and luminescence properties of Eu^{3+} in CaMoO_4 and SrMoO_4 . *Dalton Transactions* **2015**, *44*, 18957-18969.
28. Gupta, S. K.; Ghosh, P. S.; Yadav, A. K.; Jha, S. N.; Bhattacharyya, D.; Kadam, R. M., Origin of Blue-Green Emission in $\alpha\text{-Zn}_2\text{P}_2\text{O}_7$ and Local Structure of Ln^{3+} Ion in $\alpha\text{-Zn}_2\text{P}_2\text{O}_7:\text{Ln}^{3+}$ (Ln = Sm, Eu): Time-Resolved Photoluminescence, EXAFS, and DFT Measurements. *Inorganic chemistry* **2016**, *56*, 167-178.
29. Gupta, S. K.; Sudarshan, K.; Ghosh, P. S.; Mukherjee, S.; Kadam, R. M., Doping-induced room temperature stabilization of metastable $\beta\text{-Ag}_2\text{WO}_4$ and origin of visible emission in α - and $\beta\text{-Ag}_2\text{WO}_4$: low temperature photoluminescence studies. *The Journal of Physical Chemistry C* **2016**, *120* (13), 7265-7276.

30. Gupta, S. K.; Sudarshan, K.; Ghosh, P.; Sanyal, K.; Srivastava, A.; Arya, A.; Pujari, P.; Kadam, R., Luminescence of undoped and Eu^{3+} doped nanocrystalline SrWO_4 scheelite: time resolved fluorescence complimented by DFT and positron annihilation spectroscopic studies. *RSC Advances* **2016**, *6*, 3792-3805.
31. Wang, C.; Zhou, T.; Jiang, J.; Geng, H.; Ning, Z.; Lai, X.; Bi, J.; Gao, D., Multicolor tunable luminescence based on $\text{Tb}^{3+}/\text{Eu}^{3+}$ doping through a facile hydrothermal route. *ACS applied materials & interfaces* **2017**, *9*, 26184-26190.
32. Eagleman, Y.; Weber, M.; Chaudhry, A.; Derenzo, S., Luminescence study of cerium-doped $\text{La}_2\text{Hf}_2\text{O}_7$: Effects due to trivalent and tetravalent cerium and oxygen vacancies. *Journal of Luminescence* **2012**, *132* (11), 2889-2896.
33. Ji, Y.; Jiang, D.; Shi, J., $\text{La}_2\text{Hf}_2\text{O}_7:\text{Ti}^{4+}$ ceramic scintillator for x-ray imaging. *Journal of materials research* **2005**, *20*, 567-570.
34. Wang, Z.; Zhou, G.; Zhang, J.; Qin, X.; Wang, S., Luminescence properties of Eu^{3+} -doped Lanthanum gadolinium hafnates transparent ceramics. *Optical Materials* **2017**, *71*, 5-8.
35. Yanagida, T.; Okada, G., Characterizations of optical properties and radiation induced luminescence of Bi-doped $\text{La}_2\text{Zr}_2\text{O}_7$ transparent ceramics. *Journal of the Ceramic Society of Japan* **2016**, *124*, 564-568.
36. Du, M. H., Mn^{4+} emission in pyrochlore oxides. *Journal of Luminescence* **2015**, *157*, 69-73.
37. Trojan-Piegza, J.; Gierlotka, S.; Zych, E.; Lojkowski, W., Spectroscopic Studies of Nanopowder and Nanoceramics $\text{La}_2\text{Hf}_2\text{O}_7:\text{Pr}$ Scintillator. *Journal of the American Ceramic Society* **2014**, *97* (5), 1595-1601.
38. Zuniga, J. P.; Gupta, S. K.; Pokhrel, M.; Mao, Y., Exploring the optical properties of $\text{La}_2\text{Hf}_2\text{O}_7:\text{Pr}^{3+}$ nanoparticles under UV and X-ray excitation for potential lighting and scintillating applications. *New Journal of Chemistry* **2018**, *42* (12), 9381-9392.
39. Trojan-Piegza, J.; Zych, E.; Kosińska, M., Fabrication and spectroscopic properties of nanocrystalline $\text{La}_2\text{Hf}_2\text{O}_7:\text{Pr}$. *Radiation Measurements* **2010**, *45* (3), 432-434.
40. Lindfield, G.; Penny, J., Chapter 8 - Physics Inspired Optimization Algorithms. In *Introduction to Nature-Inspired Optimization*, Lindfield, G.; Penny, J., Eds. Academic Press: Boston, 2017; pp 141-170.
41. Gupta, S. K.; Sudarshan, K.; Ghosh, P.; Srivastava, A.; Bevara, S.; Pujari, P.; Kadam, R., Role of various defects in the photoluminescence characteristics of nanocrystalline $\text{Nd}_2\text{Zr}_2\text{O}_7$: an investigation through spectroscopic and DFT calculations. *Journal of Materials Chemistry C* **2016**, *4*, 4988-5000.
42. Zawisza, K.; Strzep, A.; Wiglusz, R. J., Influence of annealing temperature on the spectroscopic properties of hydroxyapatite analogues doped with Eu^{3+} . *New Journal of Chemistry* **2017**, *41*, 9990-9999.
43. Blanchard, P. E.; Liu, S.; Kennedy, B. J.; Ling, C. D.; Avdeev, M.; Aitken, J. B.; Cowie, B. C.; Tadich, A., Investigating the local structure of lanthanoid hafnates $\text{Ln}_2\text{Hf}_2\text{O}_7$ via diffraction and spectroscopy. *The Journal of Physical Chemistry C* **2013**, *117*, 2266-2273.
44. Popov, V.; Menushenkov, A.; Yaroslavtsev, A.; Zubavichus, Y. V.; Gaynanov, B.; Yastrebtshev, A.; Leshchev, D.; Chernikov, R., Fluorite-pyrochlore phase transition in nanostructured $\text{Ln}_2\text{Hf}_2\text{O}_7$ (Ln = La-Lu). *Journal of Alloys and Compounds* **2016**, *689*, 669-679.
45. Kumar, S.; Gupta, H., First principles study of dielectric and vibrational properties of pyrochlore hafnates. *Solid State Sciences* **2012**, *14* (10), 1405-1411.

46. Mathpal, M. C.; Tripathi, A. K.; Singh, M. K.; Gairola, S. P.; Pandey, S.; Agarwal, A., Effect of annealing temperature on Raman spectra of TiO₂ nanoparticles. *Chemical Physics Letters* **2013**, *555*, 182-186.
47. Xu, C.; Zhang, P.; Yan, L., Blue shift of Raman peak from coated TiO₂ nanoparticles. *Journal of Raman spectroscopy* **2001**, *32*, 862-865.
48. Luwang, M. N.; Ningthoujam, R.; Srivastava, S.; Vatsa, R., Effects of Ce³⁺ codoping and annealing on phase transformation and luminescence of Eu³⁺-doped YPO₄ nanorods: D₂O solvent effect. *Journal of the American Chemical Society* **2010**, *132*, 2759-2768.
49. Kong, L.; Karatchevtseva, I.; Gregg, D. J.; Blackford, M. G.; Holmes, R.; Triani, G., A novel chemical route to prepare La₂Zr₂O₇ pyrochlore. *Journal of the American Ceramic Society* **2013**, *96* (3), 935-941.
50. Socrates, G., *Infrared and Raman characteristic group frequencies: tables and charts*. John Wiley & Sons: 2001.
51. Nigam, S.; Sudarsan, V.; Vatsa, R. K., Effect of Annealing Temperature on the Structural and Photoluminescence Properties of Y₂Sn₂O₇:Eu Nanoparticles. *European Journal of Inorganic Chemistry* **2013**, *2013*, 357-363.
52. Singh, N. S.; Ningthoujam, R.; Yaiphaba, N.; Singh, S. D.; Vatsa, R., Lifetime and quantum yield studies of Dy³⁺ doped GdVO₄ nanoparticles: Concentration and annealing effect. *Journal of Applied Physics* **2009**, *105* (6), 064303.
53. Huang, R.; Wang, X.; Song, J.; Guo, Y.; Ding, H.; Wang, D.; Xu, J.; Chen, K., Strong orange-red light emissions from amorphous silicon nitride films grown at high pressures. *Scripta Materialia* **2010**, *62*, 643-645.
54. Huang, R.; Wang, X.; Guo, Y.; Song, J.; Zhang, Y.; Song, C., Effects of Hydrogen on Luminescence Properties of A-Sinx Films Prepared by VHF-PECVD. *Physics Procedia* **2012**, *32*, 417-422.
55. Wang, W.-N.; Widiyastuti, W.; Ogi, T.; Lenggoro, I. W.; Okuyama, K., Correlations between crystallite/particle size and photoluminescence properties of submicrometer phosphors. *Chemistry of Materials* **2007**, *19*, 1723-1730.
56. Ju, Q.; Liu, Y.; Li, R.; Liu, L.; Luo, W.; Chen, X., Optical spectroscopy of Eu³⁺-doped BaFCl nanocrystals. *The Journal of Physical Chemistry C* **2009**, *113*, 2309-2315.
57. Binnemans, K., Interpretation of europium (III) spectra. *Coordination Chemistry Reviews* **2015**, *295*, 1-45.
58. Boukerika, A.; Guerbous, L., Annealing effects on structural and luminescence properties of red Eu³⁺-doped Y₂O₃ nanophosphors prepared by sol-gel method. *Journal of luminescence* **2014**, *145*, 148-153.
59. Fu, Z.; Zhou, S.; Pan, T.; Zhang, S., Preparation and luminescent properties of cubic Eu³⁺:Y₂O₃ nanocrystals and comparison to bulk Eu³⁺:Y₂O₃. *Journal of Luminescence* **2007**, *124*, 213-216.
60. Siqueira, K. P.; Lima, P. P.; Ferreira, R. A.; Carlos, L. D.; Bittar, E. M.; Matinaga, F. M.; Paniago, R.; Krambrock, K.; Moreira, R. L.; Dias, A., Influence of the matrix on the red emission in europium self-activated orthoceramics. *The Journal of Physical Chemistry C* **2015**, *119*, 17825-17835.
61. McCamy, C. S., Correlated color temperature as an explicit function of chromaticity coordinates. *Color Research & Application* **1992**, *17*, 142-144.

62. Gupta, S. K.; Mohapatra, M.; Kaity, S.; Natarajan, V.; Godbole, S., Structure and site selective luminescence of sol–gel derived Eu:Sr₂SiO₄. *Journal of Luminescence* **2012**, *132*, 1329-1338.
63. Sudheendra, L.; Das, G. K.; Li, C.; Stark, D.; Cena, J.; Cherry, S.; Kennedy, I. M., NaGdF₄:Eu³⁺ nanoparticles for enhanced x-ray excited optical imaging. *Chemistry of Materials* **2014**, *26*, 1881-1888.
64. Gomes, M. A.; Carvalho, J. C.; Andrade, A. B.; Rezende, M. V.; Macedo, Z. S.; Valerio, M. E., Effects of X-ray irradiation on the Eu³⁺→Eu²⁺ conversion in CaAl₂O₄ phosphors. *Optical Materials* **2018**, *75*, 122-126.